Predicting Particle Deposition in the Human Airways with RANS Turbulence Modeling

BY

Hannibal Eie Fossum

THESIS

for the degree of

MASTER OF SCIENCE

(Master i Anvendt matematikk og mekanikk)

Faculty of Mathematics and Natural Sciences
University of Oslo

May 2009

Det matematisk- naturvitenskapelige fakultet
Universitetet i Oslo

Predicting Particle Deposition in the Human Airways with RANS Turbulence Modeling

by

Hannibal Eie Fossum

THESIS
for the degree of

MASTER OF SCIENCE
(Master i Anvendt matematikk og mekanikk)

Faculty of Mathematics and Natural Sciences
University of Oslo

May 2009

Det matematisk- naturvitenskapelige fakultet
Universitetet i Oslo

Abstract

Particle deposition in the lungs have so far been modeled mainly with the assumption of laminar flow. In the present study, several RANS turbulence models are used to simulate the airflow and particle deposition in the human respiratory system. The results are compared to LES reference data, and it is demonstrated that relatively simple two-equation eddy viscosity models seem adequate to reproduce the primary features of the flow field. The present study seems to suggest that the RANS approach gives realistic results for particles with diameters $d_p \geq 10$ μm.

Acknowledgments

First and foremost, many thanks to my supervisor Bjørn Anders Petterson Reif at the University of Oslo and the Norwegian Defence Research Establishment. His guidance has been very helpful throughout the research process.

Furthermore, I wish to thank Emma M. M. Wingstedt and the other researchers at the Norwegian Defence Research Establishment for helpful comments, positive feedback and useful discussions.

Communication with and data from Hari Radhakrishan have also been greatly appreciated.

My collegue Magnus Vartdal has provided me with good ideas, valuable arguments and welcome companionship.

Finally, my gratitude goes to my family and girlfriend for their support. In particular, Camilla has given me both loads of encouragement and useful corrections on my written work.

Nomenclature

The following *physical* quantities are used throughout this paper. Note that purely mathematical notation, such as unknown coefficients, example functions, indices or specific turbulence model parameters, are not included in the following. Quantities with index i refers to vector quantities, whereas index n refers to some other counting procedure. Dimensions are as listed below, except when stated otherwise in the text.

Roman Symbols

$\boldsymbol{A}$	area vector (m^2)
A_n	the area of a cell face (m^2)
C	mean part of scalar field
c	fluctuating part of scalar field
$\tilde{c}$	total instantaneous scalar field
D_{ij}	collection of transport terms for $\overline{u_i u_j}$ ($\mathrm{m}^2/\mathrm{s}^3$)
d_p	particle diameter (m)
d^k	gradient diffusion model for k ($\mathrm{m}^2/\mathrm{s}^3$)
d^p	pressure diffusion of k ($\mathrm{m}^2/\mathrm{s}^3$)
d^t	turbulent transport of k ($\mathrm{m}^2/\mathrm{s}^3$)
d^ε	gradient diffusion model for ε ($\mathrm{m}^2/\mathrm{s}^4$)
$d^{\hat{\nu}_T}$	gradient diffusion model for $\hat{\nu}_T$ ($\mathrm{m}^2/\mathrm{s}^2$)
F_D	specific Stokes drag force on a particle (1/s)
F_{x_p}	virtual mass and pressure gradient forces on a particle ($\mathrm{m/s}^2$)
G_n	airway generation number
g_i	gravitational acceleration ($\mathrm{m/s}^2$)
g_{x_p}	gravitational acceleration component in the x_p direction ($\mathrm{m/s}^2$)
J_n	the mass flux through a cell face (kg/s)
K	mean kinetic energy ($\mathrm{m}^2/\mathrm{s}^2$)
k	turbulent kinetic energy ($\mathrm{m}^2/\mathrm{s}^2$)
L	length scale (m)
$\ell_\mu, \ell_\varepsilon$	length scales in the two-layer zonal model (m)
P	mean part of pressure field ($\mathrm{kg/ms}^2$)
p	fluctuating part of pressure field ($\mathrm{kg/ms}^2$)
P_k	production of k ($\mathrm{m}^2/\mathrm{s}^3$)
P_{ij}	production of $\overline{u_i u_j}$ ($\mathrm{m}^2/\mathrm{s}^3$)
$P_{\hat{\nu}_T}$	production of $\hat{\nu}_T$ ($\mathrm{m}^2/\mathrm{s}^4$)
$\tilde{p}$	total instantaneous pressure field ($\mathrm{kg/ms}^2$)
Re	the Reynolds number (1)
Re_w	the wall distance based Reynolds number (1)
S_{ij}	mean rate of strain ($\mathrm{m}^2/\mathrm{s}^2$)
T	time scale (s)
t	time (s)

U	velocity scale (m/s)
U_i	mean part of velocity field (m/s)
U_{inlet}	mean inlet velocity (m/s)
$U_{\max}$	maximum mean inlet velocity (m/s)
U_+	dimensionless mean velocity field (1)
u_i	fluctuating part of velocity field (m/s)
$\tilde{u}_i$	total instantaneous velocity field (m/s)
$\tilde{u}_p$	fluid velocity in the x_p direction (m/s)
$\tilde{u}_{x_p}$	particle velocity in the x_p direction (m/s)
u_*	friction velocity (m/s)
$\boldsymbol{v}$	velocity vector (m/s)
v_n	velocity normal to a cell face (m/s)
$\boldsymbol{x}$	spatial vector (m)
x, y, z	spatial (Cartesian) coordinates (m)
x_i	spatial coordinate (m)
x_p	direction tangent to a particle trajectory (m)
$Y_{\hat{\nu}_T}$	turbulent destruction of $\hat{\nu}_T$ (m^2/s^4)
y_{w}	distance from the closest wall (m)
y_+	dimensionless distance from the wall (1)

Greek Symbols

α_c	scalar diffusivity (m^2/s)
ε	dissipation of k (m^2/s^3)
ε_{ij}	dissipation of $\overline{u_i u_j}$ (m^2/s^3)
λ	molecular mean free path (m)
μ	(dynamic) viscosity of air (kg/ms)
μ_T	eddy viscosity (turbulent viscosity) (kg/ms)
$\mu_{T,\text{2layer}}$	eddy viscosity as computed in the two-layer zonal model (kg/ms)
ν	kinematic viscosity of air (m^2/s)
ν_T	kinematic eddy viscosity (m^2/s)
$\hat{\nu}_T$	modified kinematic eddy viscosity (m^2/s)
ρ	density of air (kg/m^3)
ρ_p	particle density (kg/m^3)
τ	turbulent time scale (t)
τ_{w}	wall shear stress (wall friction) (kg/ms^2)
Φ_{ij}	pressure-strain correlation (m^2/s^3)
Ω_{ij}	mean rate of rotation tensor (1/s)
ω	dissipation of k per unit k (1/s)

Contents

1 Introduction

1.1 Background

Deposition of inhaled aerosols, such as particles or droplets containing bacteria or pollutants, in the human airways can lead to pulmonary diseases like asthma or emphysema, and evidence suggests that it may also be linked to the origin sites of bronchial carcinoma (Radhakrishan and Kassinos, 2008). Furthermore, when administering oral drug delivery, experiments indicate that as much as 80–90% of the medicine never reaches its target areas (Kleinstreuer et al., 2008b). For these reasons, it is of great interest to be able to predict particle deposition in the lungs. That way, targeted therapy can be improved.

Most Computational Fluid Dynamics (CFD) models have until recently assumed the airflow in the respiratory system to be laminar. This assumption holds only in the lower parts of the airways, roughly below the third branching generation, where the bronchus diameters are small. Experiments by Cheng et al. (1999), Caro et al. (2002) and others have shown that the airflow in the trachea and upper branches of the lung is turbulent. Recent computations (Radhakrishan and Kassinos, 2009) seem to indicate that turbulence may be present even in the lower airway parts. Although the local Reynolds number is too small to locally produce turbulence in the narrow bronchi, turbulence may still be advected to these regions from the upper airways, where turbulence is locally produced. Turbulent mixing greatly affects particle deposition, as turbulence allows for transverse transport of particles following the general direction of the flow. For gases such as air, dimensional analysis can be used to show that turbulent mixing dominates molecular diffusion by a factor of the order of the Reynolds number.

Radhakrishan and Kassinos (2008) performed Large Eddy Simulations (LES) of the airflow in the upper parts of the human airways, and they used this to predict particle depositions for various particle sizes. LES, however, is

computationally demanding; it requires a very fine grid close to impermeable surfaces, it needs to be resolved in time, and it requires ensemble averaging of many hundreds of breathing cycles in order to provide any useful statistics. In the present study, a selection of Reynolds-Averaged Navier-Stokes (RANS) turbulence closures have been employed to model flow in the same geometry as was used by Radhakrishan and Kassinos. The results have been compared with reference data from the aforementioned LES simulations. Even though RANS models cannot predict true laminar flow which might exist in the lower lung branches, the present study shows that this inability seems secondary for the prediction of large particle deposition, in which case inertia becomes more important.

This paper is divided into several sections. The current introduction serves as the first section. Then, secondly, the necessary theoretical basis will be established. Preliminary concepts will be introduced, and RANS turbulence modeling will be treated in detail. The theoretical section centers on the mathematics and physics of turbulent flows. In the third section, the numerical aspects of the study will be dealt with, as well as the specific setup for my simulations. The simulation results are then discussed in the fourth section, and conluding remarks are given in the fifth and last section.

1.2 Objectives

The objectives of this thesis may be summarized as follows:

1. Investigate various turbulence models, in particular with regards to applications related to the airflow in the human respiratory system.

2. Conduct numerical simulations of the flow in the airways, in which different mathematical turbulence models are used and compared to each other and reference data.

3. Look into ways of incorporating aerosol transport and deposition in the above simulations.

4. Investigate how statistically unsteady turbulent flows may be modeled by the RANS equations, and consider how this may be implemented in the above simulations.

When appropriate, I will put my research in context with other relevant studies in the same field.

2 Theory

2.1 Preliminaries

Before embarking on the objectives of this paper, some underlying concepts need to be dealt with. In particular, the concepts of *aerosols* and *turbulence* require some discussion. I will also give a brief introduction to averaging procedures, as these are commonly employed in turbulence modeling, and a definition of the summation convention used with index notation.

2.1.1 Turbulence

In a qualitative manner, a turbulent flow of a fluid can be recognized by chaotic and swirling motions, consisting of whirls and vortices on many length scales. Most real-life flows are turbulent, but some illustrative examples are smoke from a cigarette a few feet away from the smoke's origin (see Figure 2.1 on the following page), the water in a rapidly flowing river or a waterfall, or the mixing of tea and milk. The effects of turbulence are perhaps experienced most vividly in an airplane entering turbulent layers of air.

More precisely, a turbulent flow is a flow characterized by the following (Durbin and Petterson Reif, 2003, p. 2):

- High Reynolds numbers: $\mathrm{Re} = \frac{UL}{\nu} \gtrsim 10^3$, where U is a characteristic velocity scale, L is a characteristic length scale and ν is kinematic viscosity.

- Diffusion, i.e. rapid transportation and mixing of momentum, temperature, kinetic energy etc.

- Dissipation, i.e. turbulence kinetic energy is transformed into internal energy by means of deformation work by viscous stresses.

- Vortical flow structures of varying scales.
- Three-dimensional flows. Turbulence cannot sustain itself in one or two dimensions![1]

Note that the above characteristics are properties of turbulent *flows*, not fluids. It is important to be aware of this when designing or choosing among turbulence models. A flow which is not turbulent is called laminar. Both laminar and turbulent flows satisfy the continuum hypothesis (Durbin and Petterson Reif, 2003, p. 49).

Figure 2.1: Smoke illustrating the transition from laminar to turbulent flow. Photo: Jan Olav Langseth

It has been shown that any flow – laminar or turbulent – can be described fully by the Navier-Stokes equations and constitutive equations like the state or energy equation (Kundu and Cohen, 2008, p. 547). Thus, it is natural to use these equations as a starting point for developing turbulence models. The derivation of the Navier-Stokes equations can be found in any introductory book on fluid mechanics, such as that of Kundu and Cohen (2008), and it is assumed the reader is familiar with them. I will use the Navier-Stokes equations as a basis in the turbulence theory section.

Strictly speaking, the Navier-Stokes equation refers only to the equation for conservation of momentum. However, it is not uncommon to mean both the mass and the momentum conservation equations when talking about the Navier-Stokes equations in plural. I will follow the latter convention in this paper.

[1] Obviously, real two-dimensional geometries do not exist in the physical world. However, it is important to remember that one can never simplify a flow to a two-dimensional case when modeling turbulence.

2.1.2 Aerosols

When microscopic particles are dispersed in a gas, it is common to refer to them as aerosols. It is important to understand that aerosols only include particles carried by gas. The concept does not refer to e.g. particles falling through a gas or being lumped together in larger chunks. Due to this fact, aerosols are limited to particles of about 100 μm or less in diameter. Otherwise, even the lightest particles become too heavy for the gas to carry.

In fluid mechanics, the presence of aerosols is often modeled by a scalar field. The value of the field at a given point in space and time says something about the concentration of the aerosol in this point. Usually, some sort of average is taken (see Section 2.1.3), but instantaneous concentration values are also possible.

If the aerosol particles do not affect the flow field, they are often referred to as *passive* aerosols, passive scalars or passive contaminants. Aerosols which do affect the fluid flow fields are called *active scalars*.

Passive aerosols are relatively easy to model, once the flow field of the fluid is known. Since the aerosols do not affect the flow, one can compute first the flow field without regards to the aerosols and then the aerosol concentration field. The lack of effect of the aerosols on the flow field is why they are called passive, and it is also the reason for why the flow field and aerosol equations are uncoupled.

Active scalars pose a bigger problem. Here, the equations for the flow field and the concentration field are coupled and must thus be solved simultaneously.

2.1.3 Averages

An introduction to the concept of *ensemble averaging* and its relation to spatial and time averages will also be useful.

Even though turbulence is fundamentally deterministic (it *can* in theory be found from the Navier-Stokes equations), it also has a stochastic nature. That is, it is possible to say something general about turbulent structures, mean velocities, flow developments and so forth, but it is impossible to predict *exactly* how the details of the flow will look at a certain time. The latter follows from the fact that any initial and boundary condition of a problem is subject to small perturbations, and that turbulent flows display an acute sensitivity to such perturbations. Consult Pope (2000, p. 34) for a more thorough treatment of this issue.

In light of the above, we might want to use statistics to describe turbulence – and indeed we will, as shown in Section 2.3. But how should the turbulent flow be averaged?

The ideal way to find the «perfect» average of a turbulent flow would be to run infinitely many experiments with as close to identical conditions as

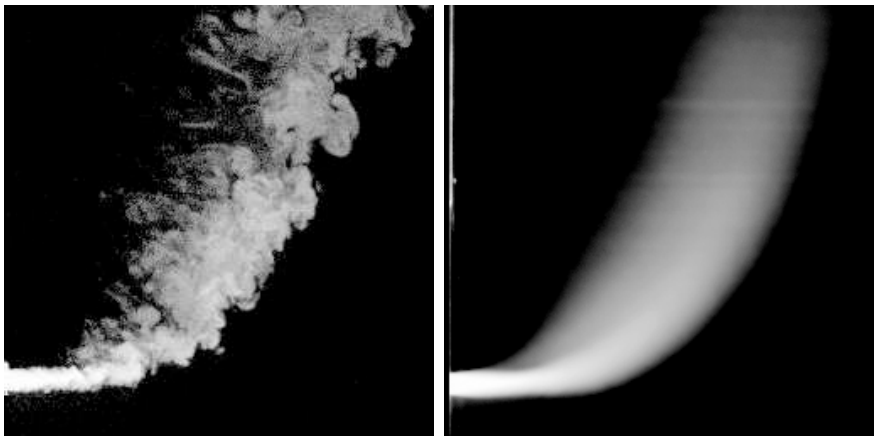

(a) Instantaneous flow field. (b) Ensemble averaged flow field.

Figure 2.2: Turbulent flow illustrated by smoke (Su and Mungal, 1999).

possible and then average the results. Thus, if $f_i = f_i(\boldsymbol{x}, t)$ represents some measured field from experiment i, we could find the average field $\overline{f}$ of all the experiments via

$$\overline{f}(\boldsymbol{x}, t) \equiv \lim_{N \to \infty} \frac{1}{N} \sum_{i=1}^{N} f_i(\boldsymbol{x}, t)$$

The above average $\overline{f}$ is called an *ensemble average* of the field f. Note that even if $\overline{f}$ still depends on space and time, *information about the individual experiments has been lost*. Namely, we are left with an expression for how the *statistics* of f vary in time and space. This means, for example, that if f_i oscillates at a low, stable frequency with the same phase in all the experiments, the ensemble average will also exhibit this property. However, if each f_i consists of rapid, varying oscillations out of phase with the oscillations of the other experiments, these will be smoothed out in the ensemble average and result in a constant mean value. Figure 2.2 illustrates this.

A problem with the above is that we can never perform infinitely many experiments. We cannot let $N \to \infty$. Instead, we have to choose N large enough to approximate the ideal average. But even N experiments can be hard to perform, especially when the conditions must be similar in each one. Fortunately, for experimental purposes, one can tie the ensemble average to the time average.

If we consider the field $f_i(\boldsymbol{x})$ at a given time as one experimental sample, we can easily collect hundreds of samples by letting one experiment run through hundreds of consecutive measurements in time. When we then average these time samples over the time period the experiment has lasted, we

find an approximation to the ensemble average, i.e.

$$\overline{f}(\boldsymbol{x}) = \frac{1}{T}\int_0^T f(\boldsymbol{x}, t)\mathrm{d}t$$

where T is a suitable time scale much larger than the time scale of any turbulent fluctuations in f. By averaging this way, we essentially average over an ensemble of times.

Note in the above that large-scale fluctuations may also disappear, depending on T. Hence, the above approach is applicable only if $\overline{f}$ is *statistically steady*, i.e. that the statistics of the fields f_i are constant in time, or vary in time on a time scale much larger than T.

As turbulence can only sustain itself in three dimensions, area averaging might not make a lot of sense. Nevertheless, one could find the equivalent of the above time average approximation in terms of spatial averages. Consider for example a pipe in which several cross-sectional cuts of data are measured through time. One could then average the results from the cross-sections and find an ensemble average of all the cross-sections, giving information about the statistics of a field in a cross-sectional cut of the pipe. This average field would vary in time, but in analogue with the previous example, we would here require a *statistically fully developed* field.

A final point on averages regards the linearity of the averaging procedure. As seen from the definitions above, averaging of any kind is a linear procedure. Thus it is easily proven that the following relations hold, e.g. for the ensemble average:

a) Linearity: $\overline{c_1 f + c_2 g} = c_1\overline{f} + c_2\overline{g}$, where c_1, c_2 are non-random constants.

b) Average of average: $\overline{\overline{f}g} = \overline{f}\,\overline{g}$

These relations will be used later, when developing the basics of turbulence modeling. A convenient notation for vector equations will also be needed, which I will touch upon briefly in the following.

2.1.4 Index Notation

When dealing with a lot of vector and tensor quantities, *index notation* is often used for simplicity. Briefly this means that if an index (marked with a subscript letter, e.g. $_i$) appears once per term in all terms of an equation, the equation holds for all values of the index that can be chosen (such as 1, 2 and 3 for three-dimensional systems). Such an index is called a *free index*. An example would be the equation $u_i = 2x_i^2$, which in three-dimensional space implies that

$$u_1 = 2x_1^2, \quad u_2 = 2x_2^2, \quad u_3 = 2x_3^2$$

In other words, the index refers to each component in a vector. The above example also brings us to one further notational convention. It is common to let $x_1 = x$, $x_2 = y$ and $x_3 = z$, where x, y and z are the standard cartesian coordinates.

In connection with index notation, I will also employ what is known as Einstein's *summation convention*: If an index appears twice in a term, this term is summed up over the range of possible index values in a given equation. For the three-dimensional case, this would for example imply that

$$u_i u_i = u_1^2 + u_2^2 + u_3^2$$

Such an index is called a *dummy index*.

In addition to the above, I will use the abbreviations $\partial_i = \frac{\partial}{\partial x_i}$ and $\partial_t = \frac{\partial}{\partial t}$.

Finally, the index notation will also be applied to tensors. It is assumed the reader is familiar with tensors and their usage. If not, the book by Kundu and Cohen (2008) is recommended for an introduction. In index notation, a tensor $\underline{\underline{T}}$ has $i \times j$ components denoted by T_{ij}.

Index notation will be used when dealing with the theory behind turbulence modeling. But first, considering the objectives of this paper, we should acquaint ourselves a bit more with the geometry of the human respiratory system.

2.2 The Flow in the Human Airways

2.2.1 Anatomy

The human respiratory system consists largely of the upper respiratory tract and the lower respiratory tract. The former includes the nasal passages, the pharynx and the larynx (vocal fold), whereas the latter is composed of the trachea (windpipe), the primary bronchi and the lungs. Figure 2.3 on the facing page illustrates these parts.

One also sometimes divides the respiratory system into functional parts, namely the conducting zone, the transitional zone and the respiratory zone. The first of these three is the region for gas transport from outside the body down to just above the alveoli and is thus the only relevant functional zone for our purposes.

Inspirational airflow passes either via the nasal passage or the mouth and then flows through the pharynx. Close to the pharynx, the epiglottis is located. The epiglottis is a fold that closes when swallowing food or drink, and it is naturally open during normal breathing. The air then flows through the larynx (the vocal chords) and down the trachea. The trachea is usually 10-12 cm long and 20–25 mm in diameter in adult humans and resembles a circular pipe. Finally, the air goes into the bronchi, which lead the flow to the pulmonary alveoli, where gas exchange with the blood occurs by means

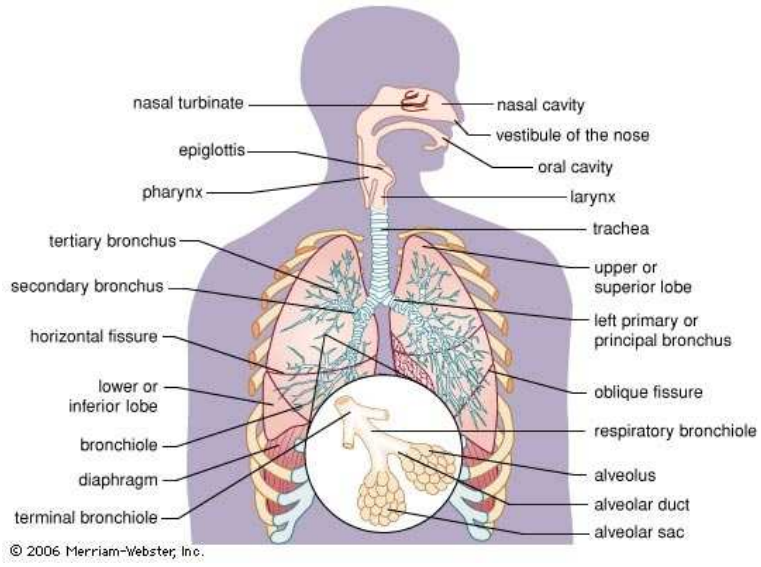

Figure 2.3: The human respiratory system and its main parts (Britannica Concise Encyclopedia).

of diffusion. Here, O_2 is deposited to the body, and CO_2 is retrieved to be transported out of the body. The right main bronchus (at the first branching of the trachea) is a bit shorter and steeper than the left (Dahl and Rinvik, 2007). This is usually neglected in computer models (see Section 2.2.2).

As mentioned earlier, the transport of aerosols is often of interest when modeling the flow in the human airways. The body must filter out as many particles as possible before the air reaches the lungs, and this process begins already in the mouth and nose. The nasal cavity captures particles bigger than about 10 μm in diameter (Slack, 2005), but the mouth has no such filtering system. However, as discussed in Section 2.1.2, aerosols are always smaller than 100 μm in diameter, so no aerosol research should consider particles larger than this.

As the air flows into the lungs, some particles are trapped in the mucus along the trachea walls and transported back up into the mouth and nose along with the mucus, while some travel all the way down to the bronchi. The particle deposition pattern depends greatly on the flow and particle size (Zhang and Kleinstreuer, 2004), and this is a subject of ongoing research. As discussed earlier, the results of such research can be of great significance when considering the administration of inhaled drugs or in the research of certain lung diseases.

A last point is worth mentioning in regard to the airflow. As the air travels toward the lungs, its temperature and humidity increases drastically. At the alveoli, the air has reached body temperature and 100% humidity

(Sand et al., 2007, p. 383). This change of physical properties may affect the flow differently than if the air was kept at constant temperature and pressure. It might be worth the time to consider this fact when modeling the flow in the airways. As the air travels out from the lungs, its properties stay roughly the same until it exits the trachea.

2.2.2 Geometrical Model

Modeling the flow in the human airways is challenging for a number of reasons, even with numerous simplifications. In this study, the dynamics of the geometry associated with moving walls have been neglected, as have the differences in temperature and humidity between the air entering the mouth and the environment in the lower bronchi. This is, at least for the upper parts of the airways, a relatively acceptable simplification.

The present geometry, also used by Radhakrishan and Kassinos (2008), is based upon measurements performed by Cheng et al. (1999). These measurements include cross-sectional areas and circumferences at different locations, and the radius of curvature in a cast of a human thorax. The upper part of the airways was created using this data. The lower part of the present airways model, i.e. the lower trachea and the branches of the lungs, were modeled with Weibel's (1963) branching model (Model A) with a branching angle of 30°. According to Radhakrishan and Kassinos, Weibel's model was scaled to match the diameter of the trachea from the thorax cast. Only the three highest branching levels were considered. In the lower branches (the fourth generation and below), the flow is laminar and thus of little interest to this study. Also, for the smaller bronchi, the effect of moving walls is no longer negligible. A picture of the actual computer model used in this study are given in Figure 2.4 on the next page. Note the indicated cut planes in the computer model, as these will be referred to later.

In Weibel's branching model, the term *generation* is used to specify the level of branching in question. The trachea is the zeroth generation, G_0, and the primary bronchi, i.e. the first branching, is considered to be the first generation, G_1. Thereafter, each branching denotes a new generation, G_n. In the non-planar model, each new branching generation is in a plane rotated 90° from the plane of the previous generation. The angle between the two branches of a generation is referred to as the *branching angle*. Each generation is similar to the preceding generation except for its size, and within each generation, each branch is considered identical to the other – the model is symmetric from G_1 downward. Note that the symmetry of the airways model constitutes a simplification of real airways.

Although natural breathing implies unsteady flow, steady inspirational breathing at a rate of 60 l/min have been considered in this study. This flow rate constitutes relatively rapid breathing. Inspirational flow has been used, as this provides the most pronounced effects of the geometric changes

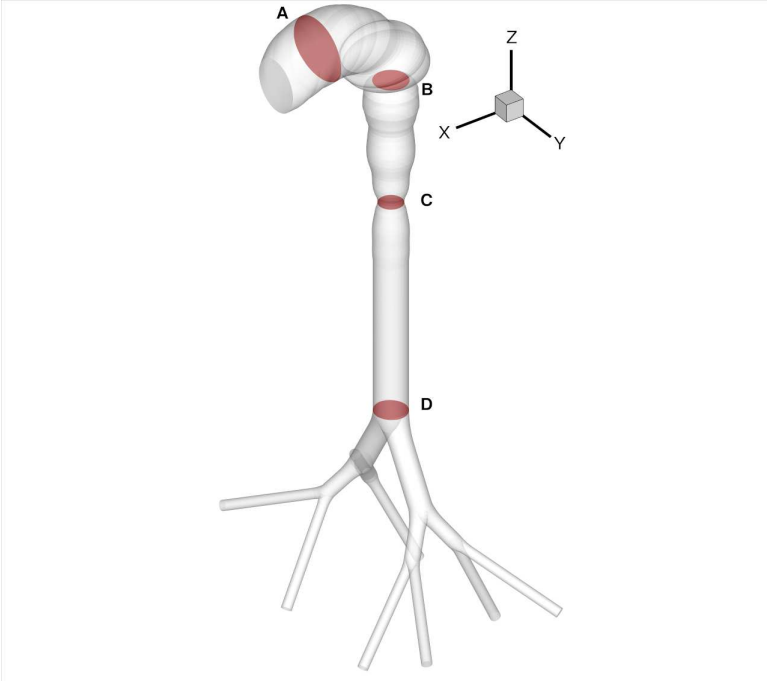

Figure 2.4: Geometrical model, shown with the cut planes used in the present study.

in the airways (Kleinstreuer et al., 2008a), and because particles enter the respiratory system through inhalation.

Previous models of the flow in the human airways have generally assumed laminar flow, such as in the simulations of Liu et al. (2002) and Comer et al. (2001a,b). In fact, though, laboratory experiments have shown the flow in the upper airways to be generally turbulent (Cheng et al., 1999). Hence, a turbulence model of the airflow will be more realistic than a laminar model, although of course more complicated as well. Dimensional analysis can be used to show that turbulent mixing is of the order of thousand times more efficient than molecular diffusion in gases such as air. This, of course, has an enourmous impact on particle deposition. In the third branching generation and below, however, the diameters of the branches are considered small enough to laminarize the flow, so models used in these lower branches may neglect turbulence effects. The two aforementioned laminar models did indeed only model G_3 and below. Recent computations (Radhakrishan and Kassinos, 2009) suggest, though, that turbulence might be advected down to the lower branches as well, so the assumption of laminar flow in those regions might not be entirely correct.

One can implement several turbulence models in order to model the flow in the airways. Choosing a model is not an easy task, nor is it inconsequential. A thorough understanding of turbulence – both physically and

mathematically – is beneficial when deciding which turbulence model to use in a simulation. This leads to the next section.

2.3 General Turbulence Modeling

As discussed in Section 2.1.1, turbulent flows as well as laminar flows are governed by the Navier-Stokes equations. That is, for incompressible, Newtonian fluids, one has the momentum conservation equation

$$\partial_t \widetilde{u}_i + \widetilde{u}_j \partial_j \widetilde{u}_i = -\tfrac{1}{\rho}\partial_i \widetilde{p} + \nu \partial_j \partial_j \widetilde{u}_i + g_i, \quad i = 1, 2, 3 \tag{2.3.1}$$

and the mass conservation equation

$$\partial_i \widetilde{u}_i = 0 \tag{2.3.2}$$

in which index notation and the summation convention is used to denote vectors and tensors.

In the Navier-Stokes equations above, $\widetilde{u}_i$ denotes the velocity field of the fluid, $\widetilde{p}$ refers to the pressure in the fluid, and ρ and ν denote the density and kinematic viscosity of the fluid, respectively. Gravitational acceleration is given by g_i. All turbulence modeling uses equations (2.3.1) and (2.3.2) as the primary basis.

If we could solve the above equations with precise boundary and initial conditions and without any simplifications or approximations, we would be finished. The solution would exhibit all characteristics of the actual flow and predict accurately the flow's development in time and space. Unfortunately, solving the above equations exactly is out of the question, both analytically and numerically. Even solving them using a direct numerical simulation approach (DNS) is extremely time-consuming and still subject to computational accuracy and knowledge of boundary conditions (White, 2006).

2.3.1 The Reynolds-Averaged Navier-Stokes Equations

Turbulent flows appear chaotic and rapidly changing, but even so, it is usually possible to recognize some steady patterns in the flow. Namely, underneath the apparent chaos of turbulence, there is a more general trend. Fortunately, when predicting fluid flow, it is often the general trends – i.e. the development of the mean values of the velocity and pressure fields – which are of interest. This motivates the implementation of *Reynolds decompositions*. Applying this concept, we separate $\widetilde{u}_i$ and $\widetilde{p}$ into one average part and one fluctuating part, i.e.

$$\widetilde{u}_i(\boldsymbol{x}, t) = U_i(\boldsymbol{x}, t) + u_i(\boldsymbol{x}, t) \tag{2.3.3}$$

$$\widetilde{p}(\boldsymbol{x}, t) = P(\boldsymbol{x}, t) + p(\boldsymbol{x}, t) \tag{2.3.4}$$

where U_i and P denote the ensemble averaged parts of the velocity and pressure fields and u_i and p denote the fluctuating parts of the fields. The latter quantities are due to turbulence, so in the case of laminar flow, U_i and P would represent the full solution.

Note that, due to the averaging process, U_i and P only vary with t if the flow is statistically unsteady. Thus, for example in a turbulent flow driven by a constant pressure gradient, U_i and P are independent of time. The averaged terms for the mean flow are obtained via ensemble averaging, i.e. $U_i = \overline{\widetilde{u}_i}$ and $P_i = \overline{\widetilde{p}_i}$ (see Section 2.1.3).

To obtain mass and momentum conservation equations for the mean velocity and pressure fields, we insert the Reynolds decompositions (2.3.3) and (2.3.4) into (2.3.1) and (2.3.2) and take the ensemble average of the resulting equations. Using the properties of the ensemble average derived in Section 2.1.3, we find

$$\partial_t U_i + U_j \partial_j U_i = -\tfrac{1}{\rho}\partial_i P + \nu \partial_j \partial_j U_i - \partial_j \overline{u_i u_j} \tag{2.3.5}$$

$$\partial_i U_i = 0 \tag{2.3.6}$$

which constitute the Reynolds-Averaged Navier-Stokes (RANS) equations, the basis for a lot of further turbulence modeling. Most modeling in this paper will also center around the above equations. A special note on the last term in (2.3.5) is appropriate at this point.

The Reynolds Stresses

The last term in (2.3.5) is the derivative of the so-called *Reynolds stress tensor*. The term originates from the advection term $\widetilde{u}_j \partial_j \widetilde{u}_i$ in (2.3.1) and is originally, after deriving (2.3.5), on the form $\overline{u_j \partial_j u_i}$. We can, however, obtain the mass conservation equation for the fluctuating field by subtracting (2.3.6) from (2.3.2). Thus we have that $\partial_i u_i = 0$, from which we see that $\overline{u_j \partial_j u_i} = \partial_j \overline{u_i u_j}$.

The Reynolds stresses are not really stresses, but they have the same dimensions as viscous stresses. The last term in (2.3.5) is unknown and arises because of the averaging process. This is a common problem when averaging non-linear equations: The very fluctuations we try to avoid by averaging come back in the form of an extra unknown variable in the averaged equation. Thus, we require extra equations in order to solve (2.3.5) and (2.3.6) completely – the problem has become unclosed. Physically, our extra term says something about the *average effect of turbulent advection on the average flow field*. In some cases it can, as mentioned, also be thought of as stresses or momentum transport.

In order to close the RANS equations, we must find a closure model for the Reynolds stresses $\overline{u_i u_j}$, and this is what contemporary turbulence research is often about – how to close the RANS equations satisfactorily?

Before moving on to this, one more concept needs to be introduced. We shall look at some useful transport equations.

2.3.2 Transport Equations

Transport equations say something about the transport or distribution of a quantity. It essentially connects the total rate of change of the quantity to the physical phenomena responsible for creating or removing the quantity.

The Reynolds Stresses

Before trying to model the Reynolds stresses, we can derive an exact equation for $\overline{u_i u_j}$. We won't be able to solve this equation, due to the many unknowns it contains. In spite of this, the equation is worth a look, as one might gain a certain physical insight from the terms contained in the equation. In addition, the equation for $\overline{u_i u_j}$ is an important part of some closure models.

If we subtract the averaged momentum equation (2.3.5) from the original momentum equation (2.3.1), we obtain an equation for the conservation of momentum for the fluctuating part of the velocity field, u_i, as given below. Note that, according to the index convention, we sum some of the terms over the dummy index k, while i is the free index.

$$\partial_t u_i + U_k \partial_k u_i + u_k \partial_k U_i + \partial_k (u_k u_i - \overline{u_k u_i}) = -\tfrac{1}{\rho}\partial_i p + \nu \partial_k \partial_k u_i \qquad (2.3.7)$$

Now, if we multiply this equation by u_j, average it and then *add* the result to the same equation as itself, only with i and j reversed, we obtain – after some algebra – the *Reynolds stress transport equation* (RSTE). It is given by

$$\begin{aligned}
\overbrace{\partial_t\overline{u_iu_j} + U_k\partial_k\overline{u_iu_j}}^{\text{total rate of change}} = &-\tfrac{1}{\rho}(\overline{u_j\partial_i p} + \overline{u_i\partial_j p}) && \text{pressure redistribution}\\
&- 2\nu\overline{\partial_k u_i \partial_k u_j} && \text{viscous dissipation}\\
&- \partial_k\overline{u_iu_ju_k} && \text{turbulent transport}\\
&- \overline{u_iu_k}\partial_k U_j - \overline{u_ju_k}\partial_k U_i && \text{production of } \overline{u_iu_j}\\
&+ \nu\nabla^2\overline{u_iu_j} && \text{molecular viscous diffusion}
\end{aligned} \tag{2.3.8}$$

in which I also have included the physical phenomenon associated with each term. For the first two terms on the right-hand side, the negative signs are *not* inherent in the physical quantities. In the remaining terms, the negative (or positive) signs stem from the expressions which represent the physical phenomena.

There are three unknowns in (2.3.8): Redistribution, viscous dissipation and turbulent transport. Turbulence models utilizing the RSTE thus have to model these terms in some way.

Turbulence Kinetic Energy

Turbulence kinetic energy is a most useful concept when trying to quantify the amount of turbulence in a flow. It represents the kinetic energy due to turbulent fluctuations and is equal to half the trace of the Reyolds stresses, i.e. $k \equiv \frac{1}{2}\overline{u_iu_i}$. Since it is a scalar, it is also relatively easy to illustrate k qualitatively (e.g. for a cross-sectional area or a simple 3D geometry) after running turbulence simulations.

The *turbulence kinetic energy equation* (TKEE) deals with the transport and distribution of turbulence kinetic energy, k, in the flow. It can be derived either directly from the Reynolds stress transport equation by means of *index contraction*, or it can be derived in a similar way as (2.3.8). The first one is the easier way: Simply let $i = j$ in (2.3.8) and use the definition of k (which essentially implies division by two). One then obtains

$$\begin{aligned}
\overbrace{\partial_t k + U_k\partial_k k}^{\text{total rate of change}} = &-\tfrac{1}{\rho}\partial_i\overline{u_ip} && \text{pressure diffusion, } d^p\\
&- \nu\overline{\partial_k u_i \partial_k u_i} && \text{viscous dissipation, } \varepsilon\\
&- \frac{1}{2}\partial_k\overline{u_iu_iu_k} && \text{turbulent transport, } d^t\\
&- \overline{u_iu_k}\partial_k U_i && \text{production of } k,\ P_k\\
&+ \nu\nabla^2 k && \text{molecular viscous diffusion}
\end{aligned} \tag{2.3.9}$$

The turbulence kinetic energy equation is important when modeling the Reynolds stresses, as will be seen later. Note the resemblance of the terms in (2.3.9) to the terms in the Reynolds stress transport equation. As with the RSTE, the first two terms on the right-hand side have their negative signs from the equations, not their physical interpretation. Mentioning this, it may also be noted that the production term P_k appears in the transport equation for the *mean* kinetic energy with the opposite sign – in other words, energy is transferred between the mean flow field and the fluctuating flow field.

If one were to solve the TKEE (2.3.9) for the mean flow field and the Reynolds stresses, there are three unclosed terms in the equation: the pressure diffusion, the viscous dissipation and the turbulent transport.

Species Transport

Finally, in light of the objectives for this thesis, the equation for the distribution of a passive contaminant will be included. Passive contaminants represent transported substances that do not affect the dynamical equations (i.e. the velocity field), such as certain pollutants, bio-areosols or chemical substances – see Section 2.1.2.

The distribution of passive contaminants is governed by advection-diffusion equations. Let $\tilde{c}$ represent the (instantaneous) scalar concentration field for the contaminant. The instantaneous advection-diffusion equation then serves as a starting point:

$$\partial_t \tilde{c} + \tilde{u}_j \partial_j \tilde{c} = \alpha_c \nabla^2 \tilde{c}$$

where α_c is the scalar diffusivity. Inserting the Reynolds decomposition $\tilde{c} = C + c$ into the above equation and averaging yields

$$\underbrace{\partial_t C + U_j \partial_j C}_{\text{total rate of change}} = \underbrace{\alpha_c \nabla^2 C}_{\substack{\text{molecular} \\ \text{diffusion}}} - \underbrace{\partial_i \overline{u_i c}}_{\text{scalar flux}} \tag{2.3.10}$$

There is one unknown term in (2.3.10), namely the scalar flux. One could now go one step further and derive the transport equation for the scalar flux. This is done similarly to the transport equation for $\overline{u_i u_j}$ (the RSTE), i.e. (i) subtract the above equation from the instantaneous-diffusion equation and multiply by u_i, then (ii) multiply the transport equation for u_i (2.3.7) by c and add it to the result of (i). This gives (next page)

$$
\begin{aligned}
\overbrace{\partial_t \overline{u_i c} + U_j \partial_j \overline{u_i c}}^{\text{total rate of change}} = & -\tfrac{1}{\rho} \overline{c \partial_i p} && \text{pressure redistribution} \\
& + \tfrac{1}{2}(\alpha_c - \nu) \partial_j (\overline{u_i \partial_j c} - \overline{c \partial_j u_i}) && \text{turbulent diffusion} \\
& + \tfrac{1}{2}(\alpha_c + \nu) \nabla^2 \overline{u_i c} && \text{molecular diffusion} \\
& - \partial_j \overline{u_i u_j c} && \text{turbulent transport} \\
& - (\alpha_c + \nu) \overline{\partial_j u_i \partial_j c} && \text{rate of dissipation of } \overline{u_i c} \\
& - \overline{u_i u_j} \partial_j C - \overline{u_j c} \partial_j U_i && \text{rate of production of } \overline{u_i c}
\end{aligned}
$$

which is referred to as the *Reynolds flux transport equation*. Several terms in this equation are usually modeled. However, just as often the scalar flux is modeled directly instead of being computed from the above equation. A simple model for the scalar flux will be shown in Section 2.6, in which equation (2.3.10) will be revisited. In Section 2.6, particle transport will also be discussed from a Lagrangian perspective.

Transport equations such as those considered here are important for our understanding of turbulence. They also play major roles in the derivation of turbulence models, which is the topic of the next section.

2.4 RANS Turbulence Models

In addition to direct numerical simulations (DNS) and large eddy simulations (LES), the RANS equations are the most known method of simulating turbulent flows. The two former techniques are generally more applicable and accurate, but they are also much more costly in terms of computer power. Both memory and CPU requirements are enormous, and DNS in particular is currently impossible to apply to real-life geometries (White, 2006). Hence, I will emply various RANS models in this thesis. Radhakrishan and Kassinos (2008) used LES to predict particle depositions in the human airways, and I will compare my RANS results to theirs in order to assess my models.

Recall that the Reynolds stresses $\overline{u_i u_j}$ represent the ensemble averaged effect of turbulent advection on the mean flow field, and keep in mind that $\overline{u_i u_j}$ is a property of the flow, not the fluid. The RANS equations contain ten unknown variables (counting each component). Since we only have four equations (again counting components), we have six unknowns that we cannot find from this system of equations. These six unknowns originates from the components of the Reynolds stress tensor, given by

$$
\{\overline{u_i u_j}\} = \begin{Bmatrix} \overline{u_1 u_1} & \overline{u_1 u_2} & \overline{u_1 u_3} \\ \overline{u_1 u_2} & \overline{u_2 u_2} & \overline{u_2 u_3} \\ \overline{u_1 u_3} & \overline{u_2 u_3} & \overline{u_3 u_3} \end{Bmatrix}
$$

and it is the eradication of these stress components from the RANS equations that is the goal of the modeling process. In other words, one wishes to model

the Reynolds stresses by using already known quantities or quantities that can be obtained through controlled experiments. Note that since the stress tensor is *symmetric* ($\overline{u_i u_j} = \overline{u_j u_i}$), we have only six unknowns, not nine.

An overview of the classes of existing turbulence models is given in Figure 2.5. I will focus on the RANS models in this study.

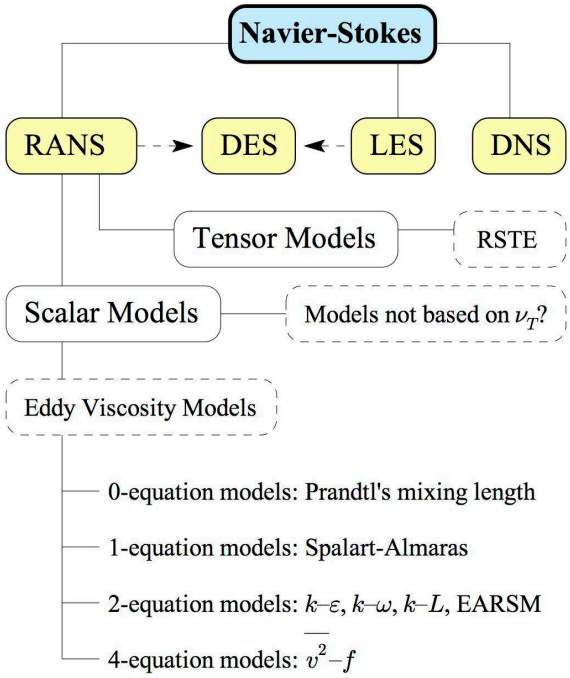

Figure 2.5: An overview of the classes of turbulence models.

2.4.1 Boussinesq's Eddy Viscosity Hypothesis

The eddy viscosity hypothesis is the basis for all scalar RANS models, and I will thus derive it here. In 1877, Boussinesq devised a model for the Reynolds stresses $\overline{u_i u_j}$, based on the mean rate of strain and two unknown constants (White, 2006, p. 441). The mean rate of strain is given by

$$S_{ij} = \tfrac{1}{2}(\partial_j U_i + \partial_i U_j) \tag{2.4.1}$$

and as seen from the definition above, the tensor is symmetric. Bossusinesq's inital ansatz was a Reynolds stress tensor of the form $\overline{u_i u_j} = f(\delta_{ij}, S_{ij})$, where δ_{ij} is simply the Kronecker delta, also known as the identity matrix. Furthermore, Boussinesq surmised that one could write

$$\overline{u_i u_j} = c_1 \delta_{ij} + c_2 S_{ij}$$

Now, by definition of the turbulence kinetic energy (cf. Section 2.3.2), we have that $\overline{u_i u_i} \equiv 2k$. Hence, we find

$$c_1 \delta_{ii} + c_2 S_{ii} = 2k \Rightarrow 3c_1 + 0 = 2k \Rightarrow c_1 = \tfrac{2}{3}k$$

where we have used the summation convention and kept in mind that $S_{ii} = 0$, which follows from the Reynolds-averaged mass conservation equation (2.3.6). The second constant, c_2, can be approached by dimensional arguments. We recognize the dimensions of $\overline{u_i u_j}$ and S_{ij} to be $\mathrm{m^2 s^{-2}}$ and $\mathrm{s^{-1}}$, respectively, and for dimensional consistency, we then require the dimensions of c_2 to be $\mathrm{m^2 s^{-1}}$. This is identical to the dimensions of viscosity. We thus define an *eddy viscosity* ν_T, and, following Boussinesq, let

$$c_2 = -2\nu_T$$

Note that neither the eddy viscosity nor the kinetic energy is known, so we still have two unknowns. However, we have reduced the problem from six to two unknowns, by creating the *linear eddy viscosity model*:

$$\overline{u_i u_j} = \tfrac{2}{3}k\delta_{ij} - 2\nu_T S_{ij} \tag{2.4.2}$$

Further scalar modeling concentrates around finding or modeling the two remaining quantities properly. There are numerous ways to do this, most of which add extra equations to the RANS system in order to close it.

2.4.2 Zero-Equation Models

Zero-equation models add no extra equations to the RANS equations. Instead, the models attempt to find algebraic expressions for the unknown constants in the eddy viscosity hypothesis. The most well-known zero-equation example is Prandtl's mixing length model. However, as this model can only be used in a few cases – mainly geometries which can be approximated as one-dimensional – I will not consider it in this paper. Consult e.g. White (2006) for details of the model.

2.4.3 One-Equation Models: Spalart-Allmaras

One-equation models add *one* extra equation to the RANS equations, and so create a larger set of equations that must be solved simultaneously. Most of these models add the time-mean equation for turbulence kinetic energy or eddy viscosity to the system, plus some algebraic formulas to model various terms. This idea has not been overly popular, due to the difficulty of finding necessary length-scale correlations for complex flows, and the fact that the model results are apparently no better than the best zero-equation models (White, 2006, p. 441).

However, a relatively new one-equation model, that of Spalart and Allmaras (1992), has made the one-equation approach a bit more common, especially as a quick way of running reasonably accurate test simulations. In this model, contrary to other one-equation models, it is not necessary to calculate a length scale related to the local shear layer thickness. In addition to the RANS equations, the Spalart-Allmaras model solves a transport equation for a modified form of the eddy-viscosity. The model is economical for large meshes, and the modified eddy viscosity is easy to resolve close to walls. This implies that the Spalart-Allmaras model is good for boundary-layer flows. The model is relatively quick to converge in a numerical solver, and I will explore the results obtained from this model in the airways geometry. The model will not be derived here, as the derivation is tedious and gives little insight compared to e.g. the $k-\varepsilon$ model, but the model equations are included in the following.

For incompressible flows, the transport equation for the modified eddy viscosity $\hat{\nu}_T$ is given by

$$\begin{aligned}
\overbrace{\partial_t \hat{\nu}_T + U_k \partial_k \hat{\nu}_T}^{\text{total rate of change}} &= c_{b1}\tilde{S}\hat{\nu}_T && \text{turbulent production, } P_{\hat{\nu}_T} \\
&+ \frac{c_{b2}}{\sigma_{\hat{\nu}_T}}(\partial_k \hat{\nu}_T \partial_k \hat{\nu}_T) && \text{model tuning term/diffusion} \\
&- c_{\mathrm{w}1} f_{\mathrm{w}} \left(\frac{\hat{\nu}_T}{y_{\mathrm{w}}}\right)^2 && \text{turbulent destruction, } Y_{\hat{\nu}_T} \\
&+ \partial_k \left(\frac{\hat{\nu}_T}{\sigma_{\hat{\nu}_T}} \partial_k \hat{\nu}_T\right) && \text{gradient diffusion model term, } d^{\hat{\nu}_T} \\
&+ \frac{\nu}{\sigma_{\hat{\nu}_T}} \nabla^2 \hat{\nu}_T && \text{molecular viscous diffusion}
\end{aligned} \tag{2.4.3}$$

Note the resemblance to the transport equations derived in Section 2.3.2. In the above equation, y_{w} is the distance from the wall. This means that the turbulent destruction term effectively removes the (modified) eddy viscosity in the viscous region close to the wall. The tuning term controls the evolution of free shear layers (Durbin and Petterson Reif, 2003, p. 140) by means of diffusion. The term can be rewritten into two diffusion terms by using the chain rule.

The modified eddy viscosity, $\hat{\nu}_T$, is identical to the turbulent kinematic viscosity except in the near-wall region. That is, in the Spalart-Allmaras model, the turbulent kinematic viscosity is given by

$$\nu_T = f_{v1}\hat{\nu}_T$$

where

$$f_{v1} = \frac{\left(\frac{\hat{\nu}_T}{\nu}\right)^3}{\left(\frac{\hat{\nu}_T}{\nu}\right)^3 + c_{v_1}^3}$$

The turbulent production term $P_{\hat{\nu}_T}$ in (2.4.3) contains a modified deformation term given by

$$\tilde{S} = S + \frac{\hat{\nu}_T}{\kappa^2 y_{\mathrm{w}}^2} f_{v2}$$

where

$$f_{v2} = 1 - \frac{\frac{\hat{\nu}_T}{\nu}}{1 + \frac{\hat{\nu}_T}{\nu} f_{v1}}$$

and S is a scalar measure of the deformation tensor based on the vorticity magnitude. In a non-rotating frame of reference, S is given by

$$S = \sqrt{2\Omega_{ij}\Omega_{ij}}$$

where $\Omega_{ij} = \frac{1}{2}(\partial_j U_i - \partial_i U_j)$ is the mean rate of rotation tensor.

In the turbulent destruction term $Y_{\hat{\nu}_T}$, which arises due to kinematic blocking and viscous damping at walls, we have that

$$f_{\mathrm{w}} = q \left[\frac{1 + c_{\mathrm{w}3}^6}{q^6 + c_{\mathrm{w}3}^6} \right]^{1/6}$$

and

$$q = \frac{\hat{\nu}_T}{\tilde{S}\kappa^2 y_{\mathrm{w}}^2} + c_{\mathrm{w}2} \left(\left[\frac{\hat{\nu}_T}{\tilde{S}\kappa^2 y_{\mathrm{w}}^2} \right]^6 - \frac{\hat{\nu}_T}{\tilde{S}\kappa^2 y_{\mathrm{w}}^2} \right)$$

The gradient diffusion term is a modeled term, and in the derivation of the $k - \varepsilon$ model in Section 2.4.4, such a model term is explained more thoroughly. Note, finally, that since no turbulent kinetic energy k is computed, the first term in the Boussinesq model (2.4.2) will be ignored. The model constants used in the above will in this study be taken as

$$c_{b1} = 0.1355, \qquad c_{b2} = 0.622, \qquad \sigma_{\hat{\nu}_T} = 2/3, \qquad c_{v1} = 7.1$$

$$c_{\mathrm{w}1} = \frac{c_{b1}}{\kappa^2} + \frac{1 + c_{b2}}{\sigma_{\hat{\nu}_T}}, \qquad c_{\mathrm{w}2} = 0.3, \qquad c_{\mathrm{w}3} = 2.0, \qquad \kappa = 0.4187$$

The special wall boundary conditions associated with the Spalart-Allmaras model are discussed in Section 2.5

Consult e.g. the Fluent 6.3 User's Guide for further details on the Spalart-Allmaras model.

2.4.4 Two-Equation Models: $k - \varepsilon$ and $k - \omega$

Not surprisingly, two-equation models add *two* new equations to the RANS equation system. The equation for turbulence kinetic energy (2.3.9) is always used. In addition, a second partial differential equation, usually involving time-mean turbulence dissipation, is included, plus some algebraic modeling formulas for certain quantities.

The most common two-equation model is perhaps the $k-\varepsilon$ model. Only the derivation of this model will be treated in detail here, as other two-equation models resemble this one. The derivation of the $k-\varepsilon$ model gives some insight into the modeling procedure and is perhaps the most intuitive of the RANS models, so I will include it in the following. I will then mention some other models and their main areas of application toward the end of this section.

The $k-\varepsilon$ model

The $k-\varepsilon$ model, presented by Launder and Spalding (1972), is the most widely used two-equation model. As it is the most simplistic treatment of this kind, it might also be the most likely to have any hope of further generality. The eddy viscosity ν_T and the turbulence kinetic energy k are determined from a set of partial differential equations, then inserted into the Boussinesq model (2.4.2), which is used in the RANS equations. All equations (RANS + the $k-\varepsilon$ equations) are solved simultaneously.

The two extra equations added by the $k-\varepsilon$ model is the turbulence kinetic energy equation and a dissipation of energy equation. Recall first the exact k-equation, i.e. the equation for transport of turbulence kinetic energy, from (2.3.9) and the notation we introduced for the various terms (see Section 2.3.2). We can write (2.3.9) in a shorter way, i.e.

$$\frac{\mathrm{D}k}{\mathrm{D}t} = P_k - \varepsilon + \nu\nabla^2 k - d^k \tag{2.4.4}$$

where, referring to some of the terms defined in Section 2.3.2, we have

P_k	$-\overline{u_i u_k}\partial_k U_i$	Production of k
ε	$\nu\overline{\partial_k u_i \partial_k u_i}$	Viscous dissipation
d^k	$\partial_i\overline{u_i p} + \frac{1}{2}\partial_k\overline{u_i u_i u_k}$	d^p - d^t (of Section 2.3.2)

If we use the linear eddy viscosity model (2.4.2) (assuming ν_T to be known) in (2.4.4) and solve (2.4.4) and the RANS equations for U_i and k, we still have two unknowns, ε and d^k. Hence, to obtain closure, we need to find expressions or equations for these variables (and somehow model the eddy viscosity ν_T). This is where the second equation in the two-equation model comes in.

First, let us have a look at the turbulent transport and pressure diffusion term, i.e. d^k. This term contains two physical phenomena that conveniently can be modeled together by a gradient transport model, given by[2]

$$d^k = -\partial_k(\nu_T \partial_k k)$$

[2]Note that the d^k model is an explicit expression, not the second equation in the $k-\varepsilon$ model.

with units of $\mathrm{m}^2\mathrm{s}^{-3}$. It is easily seen that inserting this into (2.4.4) yields

$$\frac{\mathrm{D}k}{\mathrm{D}t} = P_k - \varepsilon + \nu\nabla^2 k + \partial_k(\nu_T \partial_k k)$$

Now we can concentrate on the rate of dissipation of energy, ε. The dissipation can be modeled by its own transport equation, of a similar form as the other transport equations shown earlier. Considering homogeneous turbulence, i.e. a turbulent field where *all correlations are constant in space*, we have from (2.4.4) that

$$\frac{\mathrm{d}k}{\mathrm{d}t} = P_k - \varepsilon \tag{2.4.5}$$

Furthermore, in homogeneous turbulence, there is a state in which *the turbulent time scale τ is constant in time*, called *structural equilibrium* – or simply equilibrium. The turbulent time scale is the ratio between the existing turbulence kinetic energy and the dissipation of it, i.e. $\tau = k/\varepsilon$. In equilibrium, then, we require $\frac{\mathrm{d}}{\mathrm{d}t}(\frac{k}{\varepsilon}) = 0$. Using standard differentiation rules on this equilibrium condition, we get that

$$\frac{\mathrm{d}\varepsilon}{\mathrm{d}t} = \frac{1}{k/\varepsilon}\frac{\mathrm{d}k}{\mathrm{d}t}$$

and inserting (2.4.5) into this we observe that

$$\frac{\mathrm{d}\varepsilon}{\mathrm{d}t} = \frac{P_k - \varepsilon}{k/\varepsilon}$$

from which we can surmise that perhaps a «general» ε-equation could be conjectured, following the form of the k-equation. Thus the second equation in the $k-\varepsilon$ model is proposed as

$$\frac{\mathrm{D}\varepsilon}{\mathrm{D}t} = \frac{c_{\varepsilon 1}P_k - c_{\varepsilon 2}\varepsilon}{k/\varepsilon} + \nu\nabla^2\varepsilon + d^\varepsilon \tag{2.4.6}$$

where $d^\varepsilon \sim \partial_k(\nu_T\partial_k\varepsilon)$ is a gradient diffusion term, similar to d^k in the k-equation. Notice the similarity to the k-equation.

To summarize, the final form of the two-equation $k-\varepsilon$ model is given by the RANS equations (2.3.5) and (2.3.6), the k-equation (2.4.4) and the ε-equation (2.4.6), plus algebraic models for some of the terms in these equations, such as the Boussinesq model of the Reynolds stresses, (2.4.2). In the final version of the k- and ε-equation we also include two adjustment constants (σ_k and σ_ε) in the gradient diffusion terms to allow for flexibility in tuning the model. In most models, these constants are usually set to unity.

The eddy viscosity can be found from dimensional analysis (check the units) to be

$$\nu_T = c_\mu\frac{k^2}{\varepsilon}$$

where c_μ is an empirical constant, and the production can be shown to be

$$P_k = 2\nu_T S_{ij} S_{ji} = 2\nu_T |S|^2$$

where S_{ij} is the mean rate of strain, cf. (2.4.1). If these are inserted into the $k-\varepsilon$ model, all that remains is finding all the problem parameters, i.e. the unknown constants.

The $k-\varepsilon$ model derived here is given in full on the following page. Further modeling of the $k-\varepsilon$ equations is concerned with finding suitable constants, for which the equations below constitute the necessary basis.

The constants $c_{\varepsilon 1}$, $c_{\varepsilon 2}$, c_μ, σ_k and σ_ε are still to be determined, and they are usually found by experiments and physical reasoning. Since most RANS closure models are empirical (or at least semi-empirical), a lot of time is spent trying to «tune» the parameters of a model to suitable values, so that the model will behave as required for a given class of flows. This is a drawback inherent in all eddy viscosity models. I will not deal with any details on how the $k-\varepsilon$ constants are found, but the standard values of the constants are taken to be (Fluent 6.3 User's Guide)

$$c_{\varepsilon 1} = 1.44, \quad c_{\varepsilon 2} = 1.92, \quad c_\mu = 0.09, \quad \sigma_k = 1.00, \quad \sigma_\varepsilon = 1.30$$

The standard $k-\varepsilon$ model derived above is a robust model which is widely used. I will therefore include this model in my study, despite the fact that it is not really suited for the airways geometry, due to the presence of large streamline curvatures. Another drawback of the $k-\varepsilon$ model is that it cannot be integrated close to walls – mainly because the turbulent timescale $\tau = k/\varepsilon$ tends to zero at the wall – so wall functions need to be implemented.

The $k-\varepsilon$ Model

Equations
Reynolds-averaged **momentum** conservation equation:

$$\frac{\partial U_i}{\partial t} + U_j \partial_j U_i = -\frac{1}{\rho}\partial_i P + \nu \partial_j \partial_j U_i - \partial_j \overline{u_i u_j}$$

Reynolds-averaged **mass** conservation equation:

$$\partial_i U_i = 0$$

Transport of turbulence kinetic **energy** (k-equation):

$$\frac{\mathrm{D}k}{\mathrm{D}t} = P_k - \varepsilon + \nu \nabla^2 k + \partial_k (\frac{\nu_T}{\sigma_k} \partial_k k)$$

Transport of **dissipation** of k (ε-equation):

$$\frac{\mathrm{D}\varepsilon}{\mathrm{D}t} = \frac{c_{\varepsilon 1} P_k - c_{\varepsilon 2}\varepsilon}{k/\varepsilon} + \nu \nabla^2 \varepsilon + \partial_k (\frac{\nu_T}{\sigma_\varepsilon} \partial_k \varepsilon)$$

Explicit models
Boussinesq's eddy viscosity model:

$$\overline{u_i u_j} = \tfrac{2}{3} k \delta_{ij} - 2\nu_T S_{ij}$$

Eddy viscosity given by:

$$\nu_T = c_\mu \frac{k^2}{\varepsilon}$$

Production given by:

$$P_k = 2\nu_T S_{ij} S_{ji} = 2\nu_T |S|^2$$

where $S_{ij} = \frac{1}{2}(\partial_j U_i + \partial_i U_j)$ (mean rate of strain).

Other $k-\varepsilon$ variants

As mentioned earlier, other models exist that add two extra equations to the RANS equations. Brief descriptions of the two additional $k-\varepsilon$ variants I will test on my problem, which are both related to the $k-\varepsilon$ model, are given in the following. Details about these models can be found e.g. in the Fluent 6.3 User's Guide, the book by Durbin and Petterson Reif (2003) or the book by Pope (2000).

The $k-\varepsilon$ model with Renormalization Group methods The RNG is different from the standard model in that the equations and coefficients

are derived analytically rather than empirically. This improves predictions for highly strained flows.

The $k-\varepsilon$ model with requirements of realizability The realizable $k-\varepsilon$ model includes some changes that allow certain mathematical constraints to be obeyed, such as $0 < \overline{u_i^2} < 2k$. The model offers essentially the same benefits as the RNG model, but it is better suited for flows with separation, recirculation and streamline curvature.

The $k-\omega$ model

The $k-\omega$ model is also a widely used model, in which ε is basically replaced with the dissipation per unit energy, i.e. $\omega \propto \varepsilon/k$. As this model is usually better near surfaces such as walls, it if often more used in practice than the $k-\varepsilon$ model. The model is superior for wall-bounded boundary layer, free shear and low Reynolds number flows, and it is reported to perform better in transitional flows and flows with adverse pressure gradients. Contrary to the $k-\varepsilon$ model, the $k-\omega$ model needs no wall functions (except for computational efficiency). The major downside of the model is its sensitivity to the free-stream boundary condition for ω in free shear flows. Another drawback of the model is that it typically predicts too early and too excessive separations and flow transitions in flows where these phenomena are present.

The k-equation of the $k-\omega$ model resembles that of the $k-\varepsilon$ model (see Section 2.4.4) and is given by

$$\frac{\mathrm{D}k}{\mathrm{D}t} = P_k - \beta_* f_{\beta_*} k\omega + \nu\nabla^2 k + \partial_k(\frac{\nu_T}{\sigma_k}\partial_k k)$$

(recall the notation from the $k-\varepsilon$ derivation) whereas the ω-equation is given by

$$\frac{\mathrm{D}\omega}{\mathrm{D}t} = \frac{\alpha\omega}{k} P_k \beta f_\beta \omega^2 + \nu\nabla^2\omega + \partial_k(\frac{\nu_T}{\sigma_\omega}\partial_k\omega)$$

in which α, β, β_*, σ_k and σ_ω are constant model parameters (see the end of this section for numerical values). The turbulent viscosity is then computed as

$$\nu_T = \alpha_* k/\omega$$

where α_* is a damping coefficient used for transitional (low Reynolds number) flows, given by

$$\alpha_* = \alpha_\infty^* \left(\frac{\alpha_0^* + \mathrm{Re}_t/R_k}{1 + \mathrm{Re}_t/R_k} \right)$$

Note that for high Reynolds number flows, $\alpha_* = \alpha_\infty^*$. The quantities involved in the above are included at the end of this section.

The α factor in the coefficient of the production term of the ω-equation involves α_* and is taken as

$$\alpha = \frac{\alpha_\infty}{\alpha_*}\left(\frac{\alpha_0 + \mathrm{Re}_t/R_\omega}{1 + \mathrm{Re}_t/R_\omega}\right)$$

in which the various parameters are listed with numerical values at the end of this section. Again, for high Reynolds number flows, $\alpha = \alpha_\infty$.

The two functions f_{β_*} and f_β in the $k-\omega$ equations are given by

$$f_{\beta_*} = \begin{cases} 1 & \chi_k \leq 0 \\ \frac{1+680\chi_k^2}{1+400\chi_k^2} & \chi_k > 0 \end{cases}, \qquad f_\beta = \frac{1+70\chi_\omega}{1+80\chi_\omega}$$

in which

$$\chi_k = \frac{1}{\omega^3}(\partial_k k)(\partial_k \omega), \qquad \chi_\omega = \left|\frac{\Omega_{ij}\Omega_{jk}S_{ki}}{(\beta^*_\infty \omega)^3}\right|$$

where Ω_{ij} and S_{ij} are as defined earlier in this paper, and the other quantities are given below.

The model parameters are in this study taken to be

$$\alpha_0^* = \beta_i/3, \qquad \alpha_0 = 1/9, \qquad \alpha_\infty^* = 1, \qquad \alpha_\infty = 0.52$$

$$\beta = \beta_i = 0.072, \qquad \beta_* = \beta^*_\infty(\tfrac{4/15+(\mathrm{Re}_t/R_\beta)^4}{1+(\mathrm{Re}_t/R_\beta)^4}), \qquad \beta^*_\infty = 0.09$$

$$\sigma_k = 0.5, \qquad \sigma_\omega = 0.5, \qquad \mathrm{Re}_t = \frac{k}{\nu\omega}, \qquad R_k = 6, \qquad R_\beta = 8$$

Other $k-\omega$ variants

As for the $k-\varepsilon$ model, many modifications of the standard $k-\omega$ model have been attempted. One other variant of the $k-\omega$ will be tested in this study, namely the SST version.

The SST $k-\omega$ model Offering largely the same benefits as the standard $k-\omega$ model, the SST variant combines the standard $k-\omega$ and $k-\varepsilon$ models by using a blending function ($k-\omega$ is used near walls and $k-\varepsilon$ far from walls). The model's dependency on wall distance makes it less suitable for free shear flows, but for other flows it might be more accurate and quicker than the standard $k-\omega$.

A note on the different two-equation models

Most of the modified $k-\varepsilon$ models and both the standard and SST $k-\omega$ models perform better than the standard $k-\varepsilon$ model for low Reynolds numbers and separated flows. As mentioned earlier, however, the standard model is still very much in use, owing to its qualitative performance, robustness and

simplicity. I have not included details of all the models in this paper, but the derivation of them is usually largely similar in reasoning to that of the standard $k-\varepsilon$ model. Details can be found in e.g. Pope (2000), Durbin and Petterson Reif (2003), Fluent 6.3 User's Guide or the individual papers referred to in Table 3.1 on page 44.

Also note that other two-equation models exist, such as the $k-\omega^2$ model, the $k-L$ model or the Explicit Algebraic Reynolds Stress Model. Other higher-equation classes of scalar RANS models exist as well, for example the four-equation v^2-f model. I will not treat such models in this paper, nor will I employ them in my numerical studies.

There is, however, one quite different branch of RANS modeling yet to be explored. Widely known as second-moment closure (SMC) modeling or tensor modeling, the model uses the RSTE (2.3.8) to close the RANS equations. This alternative offers considerable benefits related to e.g. rotation and streamline curvature, and I will go through the basics of the method in the following.

2.4.5 Tensor Models

The three tensor models, also known as Second-Moment Closure (SMC) models, which will be tested use the RSTE (2.3.8) to find the Reynolds stresses directly. Each tensor model adds seven equations to the two RANS equations. These models, being tensor models, provide information about each of the nine velocity fluctuation correlations $\overline{u_iu_j}$, something the scalar models cannot do. Thus tensor models also avoid the problem of predicting isotropic turbulence in parallell shear flow, which is a problem with scalar models. Moreover, tensor models avoid the (incorrect) intrinsic assumption of eddy viscosity models that $\overline{u_iu_j}$ is locally determined by S_{ij} (so called *instantaneous equilibrium*).

Due to the extra information available about the anisotropy of the turbulence, i.e. the differences between velocity fluctuation correlations, SMC models are usually better than scalar models at incorporating effects caused by rotation or curvature – a highly relevant feature of flow in the airways. However, a problem with SMC modeling is that the additional number of coupled equations make the simulations more susceptible to instabilities in the numerical methods. Also, simulations will of course require more computational resources – according to Pope (2000), the CPU time for an SMC calculation can often be more than that of a $k-\varepsilon$ calculation by a factor of two.

We can write the RSTE (2.3.8) in a slightly different way. By using the chain rule «reversed» on the pressure redistribution term, one finds

$$-\tfrac{1}{\rho}(\overline{u_j\partial_i p}+\overline{u_i\partial_j p})=-\tfrac{p}{\rho}(\overline{\partial_j u_i+\partial_i u_j})-\tfrac{1}{\rho}(\partial_j\overline{u_ip}+\partial_i\overline{u_jp})$$

Inserting this into (2.3.8) and doing some minor rearrangements, it is seen that the RSTE can be written in the form

$$\begin{aligned}\partial_t\overline{u_iu_j} + U_k\partial_k\overline{u_iu_j} = &-\tfrac{p}{\rho}(\overline{\partial_j u_i + \partial_i u_j}) && \Phi_{ij}\\ &- 2\nu\overline{\partial_k u_i \partial_k u_j} && \varepsilon_{ij}\\ &- \overline{u_iu_k}\partial_k U_j - \overline{u_ju_k}\partial_k U_i && P_{ij}\\ &- \partial_k\overline{u_iu_ju_k} + \nu\nabla^2\overline{u_iu_j} - \tfrac{1}{\rho}(\partial_j\overline{u_ip} + \partial_i\overline{u_jp}) && D_{ij}\end{aligned} \tag{2.4.7}$$

In the above, Φ_{ij} is called the pressure-strain correlation term, ε_{ij} is the rate of dissipation of the Reynolds stresses, P_{ij} is the production of Reynolds stresses and D_{ij} is a collection of all the transport terms, namely turbulent transport by velocity fluctuations, turbulent transport by molecular diffusion and turbulent transport by pressure fluctuations.

Now, some of the terms in (2.4.7) must be modeled. There are three common models for the pressure-strain correlation, namely a linear pressure-strain model (LPS), a quadratic pressure-strain model (QPS) and a low Reynolds number ω model (Low-Re). The dissipation is modeled through the assumption of isotropic dissipation and the use of a modeled transport equation for the scalar dissipation rate. Finally, the pressure fluctuation transport and the velocity fluctuation transport terms are modeled together by a turbulent diffusive transport term, similar to the method in the $k-\varepsilon$ model. The last term in D_{ij} does not need modeling, as it contains the variable one is solving for.

Further details about the SMC models described above can be found in e.g. the Fluent 6.3 User's Guide or the book by Pope (2000).

2.5 Wall Treatment

There are several ways to treat the effects of walls on turbulence. It is clear that, as for laminar flows, there is a no-slip condition on the walls, preventing any velocity in wall-adjacent cells. However, for turbulent flows, the velocity profile near the wall is hard to predict, as the velocity fluctuations is influenced by effects such as viscous damping and kinematic blocking. The former reduces tangential fluctuations, while the latter reduces normal fluctuations.

For some turbulence models, such as the $k-\omega$ models, the flow characteristics near walls can be found simply by integrating the equations all the way to the wall – as long as the grid is fine enough to capture the effects of the viscous layer close to the wall. Unfortunately, such integration is not possible for models such as the $k-\varepsilon$ or SMC models. There are many reasons for this, but the most important one is perhaps that the turbulent timescale $\tau = k/\varepsilon$ tends to zero at walls. Also, the model constants will generally not

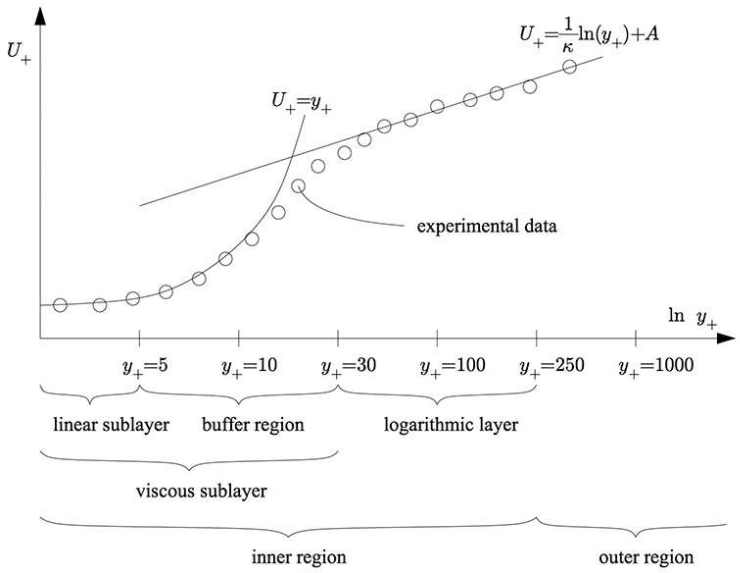

Figure 2.6: A schematic overview of the turbulent regions of wall bounded flows. (Experimental data is only exemplified.)

be valid for near-wall calculations (Pope, 2000). Hence, for such turbulence models, the problem needs to be solved in another manner.

The most common industrial approach is to use standard wall functions (Durbin and Petterson Reif, 2003; Pope, 2000; White, 2006), which essentially employs a linear velocity profile very close the wall (if the grid is fine enough) – in the so-called *viscous sublayer* – and a logarithmic profile a little bit farther from the wall – in the *log layer*. The former relation is given by

$$U_+ \approx y_+$$

whereas the latter relation, known as the *law of the wall* or the *log-law*, is given by

$$U_+ = \frac{1}{\kappa}\ln(y_+) + A$$

where A and κ are constants. Note the dimensionless quantities $U_+ = U/u_*$ amd $y_+ = yu_*/\nu$, in which $u_* = \sqrt{\tau_\mathrm{w}/\rho}$ (where τ_w is the wall friction, i.e. wall shear stress). These variables are scaled to simplify the Navier-Stokes equation for wall-bounded flows, so that y_+ equals one Kolmogorov scale, i.e. the smallest turbulent length scale (below which all energy is dissipated). The transition between the viscous sublayer and the log layer lies around $y_+ \approx 30$. Figure 2.6 show the different wall regions and the relevant relations for flows close to a straight, smooth wall.

Unfortunately, the law of the wall holds only for a few very simple flows, such as e.g. turbulent fully developed plane channel flow. Therefore, a two-layer zonal model will be used in this study. The specifics can be found in

the Fluent 6.3 User's Guide, but the two-layer model will be roughly outlined here.

In the two-layer zonal model, the flow domain is divided into the viscosity-affected region close to walls and the fully-turbulent region farther from walls. In the latter region, the standard model (e.g. the $k-\varepsilon$ or SMC model) is used. In the viscous-affected region, though, the one-equation model of Wolfstein (1969) is used. In this model, the k-equation and the momentum equations are the same as in the chosen standard turbulence model, but the turbulent viscosity formulation is different, namely

$$\mu_{T,\mathrm{2layer}} = \rho c_\mu \ell_\mu \sqrt{k}$$

where ℓ_μ is a length scale depending on the distance from the nearest wall, y_w, and the turbulent wall-distance-based Reynolds number, $\mathrm{Re}_\mathrm{w} = \frac{y_\mathrm{w}\sqrt{k}}{\nu}$. Re_w also determines the point at which the turbulence model changes between the standard model and the one-equation model: For $\mathrm{Re}_\mathrm{w} < 200$, one assumes near-wall viscosity effects, and the one-equation model is used. For $\mathrm{Re}_\mathrm{w} > 200$, the region is supposed to be fully turbulent, and the standard model equations are used. The dissipation rate in the viscosity-affected layer is given algebraically, as $\varepsilon = k^{3/2}/\ell_\varepsilon$, in which ℓ_ε is a length scale computed similarly to ℓ_μ.

The solution from the viscosity-affected region is blended with the solution from the fully-turbulent region through a blending function.

In the case where the grid is not fine enough to resolve the viscous sublayer – either through integration, as for the $k-\omega$ and Spalart-Allmaras models, or through the two-layer zonal model given above, as for the $k-\varepsilon$ and SMC models – enhanced wall function will be used. Enhanced wall functions differ from the standard wall functions mentioned earlier, in that they blend a modified version of the linear (laminar) wall velocity profile with a modified version of the logarithmic law of the wall velocity profile, using a special blending function. The mesh used in this study, however, is fine enough to avoid the use of enhanced wall functions. Thus only the pure two-layer zonal model outlined above will be used.

Note that, for the Spalart-Allmaras model, the modified turbulent viscosity is set to zero at walls. In this study, as the computational mesh will be fine enough to resolve the laminar sublayer, the wall shear stress will be obtained from the laminar stress-strain relationship, i.e.

$$\frac{u_\mathrm{wall}}{u_*} = \frac{u_* y_\mathrm{w}}{\nu}$$

where u_wall is the velocity parallell to the wall.

2.6 Particle Transport and Deposition

In this study, two different models will be used to investigate particle transport. First, a passive scalar concentration field will be superimposed on the already known flow field. The development of the mean concentration field C is governed by the transport equation (2.3.10) which was derived in Section 2.3.2.

In Section 2.3.2, however, an equation for the scalar flux was also derived. To simplify the computations somewhat, one often models the scalar flux directly, and that will be done in my simulations as well. The scalar flux will in this study be modeled in a very simplified manner, i.e. $\overline{u_i c} = \mu_T \frac{\partial C}{\partial x_i}$.

The main goal of the scalar simulation is to compute how air containing a dilute dispersion of particles will spread down into the respiratory system. Hence, once the flow field of clean air is found from equations (2.3.5) and (2.3.6), equation (2.3.10) will be solved for a mean scalar field C representing polluted air. The polluted air is modeled with the exact same properties as air. In other words, the propagation of (polluted) air in (clean) air will be simulated. The approximation of pulluted air being similar to clean air is valid, since the few particles in the polluted air change the properties of the fluid only insignificantly. For example, assuming the particles to be droplets of liquid with the density of water, the density of polluted air with 1 ppm water changes from clean air only by 0.08%.

In addition to predicting the concentration field of polluted air as described above, a set amount of *discrete* particles will also be injected at the inlet. Discrete particles are easier to model when prediciting deposition, and the discrete model also incorporates inertia effects ignored by the scalar transport model. Therefore I have focused mainly on the discrete approach in this paper. Each of the discrete particles will be tracked through the domain, so that the paths of individual particles may be estimated. The displacement of a given particle follows from integrating the force balance on the particle, which can be written in a Lagrangian reference frame. In the x_p direction of the reference frame, i.e. tangent to the particle trajectory, the force balance can be written as

$$\frac{\mathrm{d}\widetilde{u}_p}{\mathrm{d}t} = F_D(\widetilde{u}_{x_p} - \widetilde{u}_p) + \frac{g_{x_p}(\rho_p - \rho)}{\rho_p} + F_{x_p} \tag{2.6.1}$$

Here, $\widetilde{u}_{x_p}$ and $\widetilde{u}_p$ is the fluid and particle velocity, respectively, in the x_p direction. F_D is the drag force in the x_p direction, ρ and ρ_p are the densities of the fluid and the particle, respectively, and g_{x_p} is the gravitational acceleration in the x_p direction. F_{x_p} takes into account pressure-gradient and virtual mass effects. In the case studied within in this paper, thermophoretic forces, brownian forces and lift forces are assumed to have negligible effects. The ordinary differential equation (2.6.1) is solved by implicit Euler integration

or trapezoidal integration, depending on a stability condition related to how far the particle is from hydrodynamic equilibrium.

The drag force is modeled by the Stokes drag, i.e.

$$F_D = \frac{18\mu}{C_c \rho_p d_p^2}$$

in which d_p is the diameter of the particle, and C_c is the Cunningham correction computed from

$$C_c = 1 + \frac{2\lambda}{d_p}(1.257 + 0.4e^{-(1.1 d_p/2\lambda)})$$

where λ is the molecular mean free path. For standard pressure conditions, the Cunningham correction is significant only for submicron scales.

The term F_{x_p} incorporates forces induced by so-called *virtual mass* and pressure gradients in the fluid, and it is given by

$$F_{x_p} = \frac{1}{2}\frac{\rho}{\rho_p}\frac{\mathrm{d}}{\mathrm{d}t}(\widetilde{u}_{x_p} - \widetilde{u}_p) + \left(\frac{\rho}{\rho_p}\right)\widetilde{u}_{p,i}\frac{\partial \widetilde{u}_{x_p}}{\partial x_{p,i}}$$

It should be realized that many simplifications are used in the particle transport model: By considering the particles individually and assuming constant size, effects such as evaporation, agglomeration and particle collisions are neglected. Such expansions of the model could be made in later work, but in the case of rapid breathing and low-density particle systems, the simplifications applied in this study provides a good starting point.

2.7 Unsteady RANS Modeling

Unsteady RANS modeling can be used when the statistics of a flow vary in time. The governing equations are as given in (2.3.5) and (2.3.6), in which a nonzero time-derivative term in (2.3.5), i.e. $\partial_t U_i$, signifies an unsteady – or transient – mean flow field.

The turbulence models already discussed can be applied to the unsteady RANS model as well. The numerics of unsteady RANS modeling resembles that of steady state RANS modeling, only with an additional numerical scheme for the time advancement – usually a finite difference scheme, such as the backward Euler scheme or the second-order discretization scheme.

It is worth mentioning that even for flows assumed to be steady-state, unsteady RANS might provide useful. Some turbulent flows, such as flows through domains with many obstacles, might never stabilize to one flow pattern. This means that the mean flow itself will oscillate back and forth between two or more states, which might affect quantities such as mean wall shear stress per time. Moreover, for unsteady flows such as this, it is unlikely that a converged solution can ever be found, since there is no steady state to converge to.

I will focus on steady state RANS simulations in this paper, but one unsteady simulation has been done. It is outlined in Section 3.2.4, and the results are commented on in Section 4.2.

3 Numerical Method

3.1 Computational Fluid Dynamics (CFD)

3.1.1 The Finite Volume Method

The Finite Volume Method (FVM) is by far the most common numerical method in Computational Fluid Dynamics (CFD). The approach is quite similar to the Finite Difference Method (FDM), whereas it differs quite a bit from the Finite Element Method (FEM) commonly used in solid mechanics.

In the FVM, the physical domain is divided into several smaller computational cells - or data cells - arranged in what is referred to as a computational *mesh* or *grid*. These cells can be thought of as control volumes over which conservation equations are solved to obtain a solution. The variable or quantity one solves for is stored in a data point located in the center of the cell. The cells are assumed to be very small compared to gradients of velocity, pressure and other scalars, so that the entire cell can be assumed to be of one value when doing computations. However, note that even though a variable is assumed constant through an entire cell, gradients and values between cell centers can be obtained through interpolation when required!

When solving the conservation equations for mass, momentum and other scalars for a complex geometry, one essentially tries to satisfy the conservation equations for each control volume. The procedure can be outlined as follows:

1. The geometry is divided into smaller computational cells by a process called meshing (this must be done manually prior to the actual numerical solution).

2. The governing conservation equations are integrated over each control volume (i.e. each computational cell), thereby constructing discretized algebraic equations for the discrete dependent variables (velocities, pressure, temperature, scalars).

3. The discretized equations are linearized, and the resulting linear system is solved to yield updated values of the dependent variables. The linearization is acceptable, since the cells are small.

In this study, Fluent (see Section 3.1.3) solves the linear system of equations through a Gauss-Seidel linear equation solver, in conjunction with an algebraic multigrid method. Fluent is also used with the pressure-based segregated solver. In this approach, one first solves the coupled equations (momentum and mass) in a decoupled manner and then uses a pressure correction equation (obtained from the computed mass flux and velocity field) to find the pressure field. While this method is slower than a true coupled solver, it uses much less memory. To obtain values at cell faces (required e.g. for scalar flux computations) an upwind second-order scheme is used (except when it comes to pressure values, which are interpolated in a somewhat different way, using momentum equation coefficients). Gradients are computed by linearly interpolating the values at two neighboring cell centers, i.e. through an arithmetic average.

As an example of the solution procedure outlined above, consider the general mass conservation equation. On integral form, it reads

$$\oint \rho \boldsymbol{v} \cdot \mathrm{d}\boldsymbol{A} = 0$$

in which $\boldsymbol{A}$ is the area (with direction of the area normal vector) of a given control volume's boundary. For a specific cell, the above equation can be integrated over an entire computational cell, giving the discrete equation

$$\sum_{f}^{N_{\text{faces}}} J_f A_f = 0$$

where J_f is the mass flux through face f, i.e. ρv_n (in which v_n is the velocity normal to face f). J_f is computed somewhat differently from other cell face values, to avoid an unphysical phenomenon called *checkerboarding* of the pressure (in which the pressure variations are step-shaped instead of smooth). Namely, J_f is found from a momentum-weighted average, using weighting based on a coefficient from the linearized discretized momentum equation.

When solving a problem with the FVM, the solution is obtained iteratively. Therefore, the system of equations must be solved several times, using the most recent old solution as a basis for a new one. A solution procedure might require several thousands of iterations, depending on the accuracy requirements. Also, before beginning the solution procedure, i.e. before doing the first iteration, the solution must be initialized. This basically means that one must provide the solver with some inital guess of the solution, on which the algorithm can base its consecutive computations. Often the solution is

initialized at zero, but ideally the initialization should be based on an educated guess as close as possible to what the real solution should look like – this results in a more efficient solution of the problem.

3.1.2 Convergence

Since the actual correct solution to a CFD problem seldom is known, it is not possible to accurately predict the numerical error in the computations. However, several measures exist to determine the estimated error. One of the more common ones is that of residuals. Briefly, the residual says something about the imbalance between two values which should be equal – a smaller difference imply that the solution is nearing convergence. However, one can not know for certain if the solution has converged to the correct result – physical interpretation is needed to establish this. If the residuals between consecutive iterations approaches a finite value, the solution is said to be *converged*.

If computers had infinite precision, the residuals should have approached zero when nearing convergence. As computers have finite precision, though, a stabilization of residuals at a small enough value implies convergence. As long as the residuals generally decrease for each iteration, one is usually approaching a stable solution – but not always! If the residuals constantly increase or fluctuate, a solution cannot be found with the chosen numerical and/or mathematical model, and the solution is referred to as *diverging*.

In Fluent, the continuity residual is found by summing the excess mass creation over all cells. The momentum conservation residual is found by summing the imbalances in the linearized discretized momentum conservation equation over all cells. Other scalar quantities have their residuals computed similarly to momentum.

The residuals should be seen in comparison with some relevant value. Therefore, scaled residuals are usually used. In Fluent, the scaled residuals for continuity give the residual for a given iteration compared to the largest residual out of the first five iterations of the solution procedure. The scaled residuals for momentum (and scalar) conservation compares the residual for a given iteration to a factor representative of the flow rate of the scalar (or, in the case of momentum, velocity component) through the domain. More details can be found in the Fluent 6.3 User's Guide.

3.1.3 Fluent 6.3

In this study, the commercial solver Fluent 6.3 is used to compute flow fields and particle trajectories. Fluent 6.3 utilizes the Finite Volume Method and is a software tool commonly used in the CFD industry. Other similar CFD software packages include e.g. CFX or STAR-CD. More details about the

Table 3.1: RANS closures to be tested (Fluent 6.3 User's Guide)

Case	Model	Class
I	Spalart-Allmaras (Spalart and Allmaras, 1992)	Scalar, 1-eqn.
II	Standard $k-\varepsilon$ (Launder and Spalding, 1972)	Scalar, 2-eqn.
III	RNG $k-\varepsilon$ (Yakhot and Orszag, 1986)	Scalar, 2-eqn.
IV	Realizable $k-\varepsilon$ (Shih et al., 1995)	Scalar, 2-eqn.
V	Standard $k-\omega$ (Wilcox, 1998)	Scalar, 2-eqn.
VI	SST $k-\omega$ (Menter, 1994)	Scalar, 2-eqn.
VII	Reynolds Stress Model (Gibson and Launder, 1978; Launder, 1989a,b) (LPS)	Tensor, 7-eqn.
VIII	Reynolds Stress Model (Gibson and Launder, 1978; Launder, 1989a,b) (QPS)	Tensor, 7-eqn.
IX	Reynolds Stress Model (Gibson and Launder, 1978; Launder, 1989a,b) (Low-Re ω)	Tensor, 7-eqn.

specific solver options of Fluent used in this study can be found in Section 3.2.3.

3.1.4 Closure Models

The RANS closure models considered in this paper are listed in Table 3.1. Details can be found in previous sections of this paper.

As the commercial CFD software ANSYS Fluent 6.3 have been used to perform the simulations in this study, Fluent's implementation of the models in Table 3.1 have been used. The theory behind the models is described by Pope (2000), Durbin and Petterson Reif (2003), and in the Fluent 6.3 User's Guide, among others. Some details, and an example of a model derivation, can also be found in Section 2.4 of this paper. Specific values of the model constants used in the present study can be found in the Fluent 6.3 User's Guide.

Except for the modifications listed in Table 3.2, all models have been employed with Fluent's standard options. All of the special options indicated in Table 3.2 are selected mainly due to two reasons: The laminarization that takes place in the lower airways is accounted for by the Transitional Flows option (by introducing a damping of the turbulent viscosity in the model equations – see Section 2.4.4), and the need for accurate near-wall modeling leads to the use of Enhanced Wall Treatment (see Section 2.5). The Pressure Gradient Effects option only modifies one term of the enhanced near-wall function of the EWT model, so that pressure gradient effects are incorporated in the enhanced wall functions. Due to the high resolution of my mesh, though, enhanced wall functions will likely not affect the final

Table 3.2: Alterations of Fluent's standard model options

Case	Option
II	Enhanced Wall Treatment (EWT) with Pressure Gradient Effects (PGE)
III	EWT with PGE
IV	EWT with PGE
V	Transitional Flows
VI	Transitional Flows
VII	Linear Pressure-Strain with EWT and PGE
VIII	Quadratic Pressure-Strain with Non-Equilibrium Wall Functions
IX	Low-Re model with Transitional Flows

solution. PGE was nevertheless enabled, to make sure that pressure gradient effects were included in possible coarse parts of the mesh.

3.2 Pre-Processing

3.2.1 Physical Dimensions

The airways geometry is contained in a cube of approximate dimensions (in cm) $(\Delta x, \Delta y, \Delta z) = (8.7, 14, 18)$, where Δz represents the height, i.e. the axial direction of the trachea. The inlet diameter is about 2.3 cm, and each of the eight outlets has a diameter of about 0.88 cm. The length of the straight part of the trachea (from the epiglottis down to the first bifurcation) is about 16 cm.

3.2.2 Mesh Generation

To employ the Finite Volume Method of Section 3.1.1, a geometry needs to be divided into smaller cells. This process is called *meshing*, and the resulting meshed geometry is referred to as a mesh. Naturally, a given geometry can be meshed in hundreds of ways, but it turns out – not surprisingly – that some meshes are better than others.

In fact, for any CFD simulation, the quality of the mesh is vital. As one has not yet been able to make adequate automatic mesh generators, almost all meshing must be done manually. The meshing procedure is costly; usually more than half the project time for a CFD case goes to meshing.

Often, CFD algorithms will only converge toward a solution if the mesh is of sufficient quality. Moreover, even if a solution can be found, the results from a CFD simulation cannot be relied upon unless the mesh satisfies a

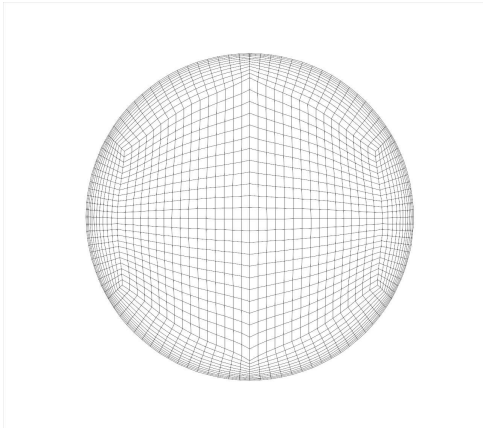

Figure 3.1: The computational mesh at the inlet.

number of requirements. These requirements are highly problem-dependent, and knowledge of fluid mechanics is essential when considering the mesh setup. Examples of mesh requirements are the need to have well-shaped cells (little skewness), no big volume differences between adjacent cells, and the need for smaller cells near impermeable surfaces.

In order to minimize computation time, a structured mesh has been used in this study. A structured grid also allows for more control over the numerical instabilities (numerical diffusion) which occurs during the computations. The volume of the geometry shown in Figure 2.4 on page 17 was meshed with hexahedral cells.

Several grids were tested to ensure grid-independent solutions, and the mesh finally used for the simulation results reported here consisted of about 480,000 cells.

The maximum permitted cell size overall was specified as 0.2 cm in any direction, but this was only a limiting factor in the streamwise direction. In the circumferencial direction, the node count on the inlet was 118, resulting in cell lengths of about 0.06 cm. At each of the eight outlets, 28 nodes were placed, also giving an approximate circumferencial cell length of 0.06 cm.

An O-grid was implemented in the main flow direction to avoid obtuse cell angles (see Figure 3.1). Very obtuse or acute cell angles should be avoided because they reduce numerical accuracy. Also, a dense boundary layer mesh was employed normal to the walls. The first layer, i.e. the wall-adjacent cells, had a height (from the wall) of 0.005 cm. A growth rate of 1.2 was used for the following ten cells, resulting in a boundary layer of approximately 0.16 cm. The cells further from the wall was set to have a maximum size of 0.1 cm. The mesh is shown in Figure 3.2 on the next page. A detailed illustration of the grid at the inlet (i.e. the mouth) is shown in Figure 3.1.

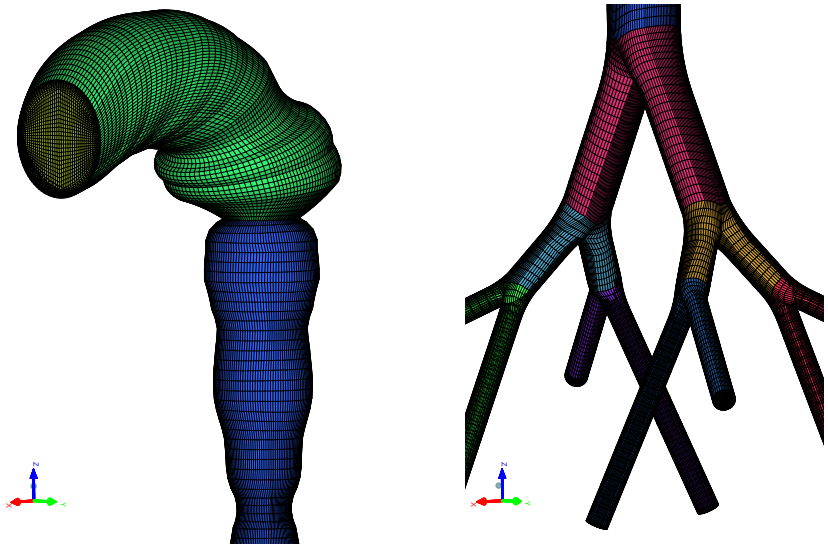

Figure 3.2: The lower and upper parts of the computational mesh.

The above specifications were determined partly through test simulations and partly through considerations of the turbulent scales. For all the simulations considered, Enhanced Wall Treatment (EWT) was used for maximum accuracy in the calculations close to walls (see Section 2.5). In order to get the best results out of EWT, it was required that the wall-adjacent cell center was within a few Kolmogorov-scales from the wall. More specifically, $y_+ = \frac{yu_*}{\nu}$, where $u_* = \sqrt{\tau_w/\rho}$ is the friction velocity and τ_w is the wall shear stress, should be within $y_+ \lesssim 5$ for all wall-adjacent cells. Using the definition of y_+, analytical calculations on circular pipes and test simulations to determine wall shear stresses, the discussed mesh requirements were found. Later simulations showed that the y_+ requirement was then indeed satisfied, as is exemplified in Figure 3.3 on the next page. Only the representative simulations I, II, V and VII are shown in this figure, so that the results are easier to see. However, the other simulations showed similar results. The highest values of y_+ were found in the cells adjacent to the glottis wall, where $y_+ \approx 2$.

3.2.3 Solver Options

Fluent employs the finite volume method (FVM) to solve the required partial differential equations as algebraic equations. The pressure-based solver was used with its standard options for all simulations. Fluent's upwind second-order discretization schemes were used to solve the equations of momentum, as well as the model equations involved in the RANS model.

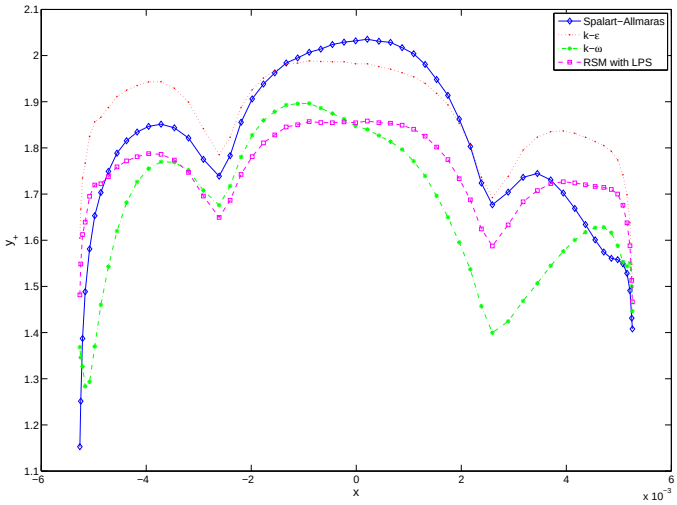

Figure 3.3: Values of y_+ at the glottis wall for cases I, II, V and VII.

To obtain the desired breathing rate, a uniform inlet velocity of 2.4 m/s was chosen. For the 2.3 cm inlet diameter, this corresponds to about $\mathrm{Re} = 3800$, i.e. a turbulent low Reynolds number flow. However, the Reynolds number at the inlet should not be given too much weight, since the geometry changes a lot downstream, and it is not the oral cavity that it the most important region in this study. For each of the outlets, a pressure-outlet boundary condition was used, with a zero gauge pressure relative to the operating pressure. In case of any backflow, i.e. reversed flow, the backflow direction for a given cell was set to be calculated from the flow direction in the neigboring cells.

The fluid region was specified as air with Fluent's standard parameters of $\rho = 1.225$ and $\mu = 1.7894 \cdot 10^{-5}$. Gravitational acceleration was set to $g_i = (0, 0, -9.81)$ m/s^2 and the operating pressure and temperature were set to 101.325 kPa and 300 K, respectively.

The passive scalar transport was modeled with Fluent's Species Transport Model, with two species, (clean) air and (polluted) air, as discussed earlier. An initial polluted air mass fraction of 1, i.e. 100%, was specified at the inlet at time $t = 0$ and the propagation of the polluted air was predicted through time. A time step size of 0.002 s was used. Note that while the concentration was studied in time, the flow was steady.

For the discrete particle transport, Fluent's Discrete Phase Model was used, without coupling between the continuous and the discrete phase. Fluent's model is based on equation (2.6.1). The modeled species was specified as inert droplets of water with an estimated Cunningham factor of $C_c = 1$. Separate simulations were performed for particles with diameters of 1, 10

and 20 μm. The particles were released from four different uniformly spaced grid planes at the inlet. For each of the planes, two (in one case three) releases were simulated, adding up to a total of nine particle releases per type of particle.

Turbulent fluctuations in the particle transport were accounted for by using Fluent's Discrete Random Walk (DRW) model, in which the eddy sizes affecting the particle tracks were calculated from the flow simulation results. The DRW model was used with standard options, except for enabling random eddy lifetime. The computational spatial step for the particle calculations was set to 0.05 cm. To account for the presence of mucus on the trachea and bronchus walls, particle entrapment at the walls was enabled.

Only the realizable $k-\varepsilon$ turbulence model (case IV) was used to simulate particle transport, as it gave the best overall results for the single flow simulations (as compared to the LES data).

3.2.4 Unsteady RANS

In the unsteady RANS simulations, it is assumed that one full breathing cycle (in and out) lasts for π seconds, implying a breathing rate of about 19 cycles per minute. The maximum velocity for a given cycle is assumed to be 2.4 m/s (as for the steady state simulations), and the inlet velocity is assumed to be spatially uniform. That way, the transient simulation will resemble the steady state simulation as much as possible. More specifically, the inlet velocity for the transient case is given as

$$U_{\text{inlet}} = U_{\max} \sin(2t)$$

in which $U_{\max} = 2.4$ m/s and t is time. The implementation of this velocity profile was written in C++ code and used in Fluent as a so-called User-Defined Function. The C++ code can be found in Appendix A.

For the unsteady simulation, the realizable $k-\varepsilon$ model was used, as it was the most promising model for the steady state case (see Section 4.1.1). An implicit scheme, which is unconditionally stable, was used with a time step of $\Delta t = 6.2832 \cdot 10^{-3}$. Thus, the 500 time steps that were simulated correspond to one breathing cycle.

Also, for the transient case, a (passive) scalar concentration field was simulated. Initially, the inlet was assumed to have a 100% concentration of polluted air while the rest of the geometry contained only clean air. Then, the propagation of the polluted air was studied in time. This case differs from the steady state scalar field simulation in that also the flow field now varies in time.

4 Results

4.1 Steady State Solutions

4.1.1 Airflow

Flow simulations for all the RANS models listed in Table 3.1 were performed. Except for case IX, all simulations produced reasonable physical results. The reason for the deficiency of case IX is not presently known. The Spalart-Allmaras method of case I is inferior to the others, due to its lack of information about turbulent scales (thus preventing the use of e.g. the DRW model), but it produced the same flow predictions as the other methods.

Qualitative considerations indicated that the results of case IV showed the closest likeness to the LES data of Radhakrishan and Kassinos (2008). Case IV also agreed well with the tensor models of case VII and VIII. Only case IV was therefore used in the modeling of the species transport, and hence only this case is considered in the following. Most of the other simulations gave similar results to case IV, only slightly differing from the one discussed here.

It is interesting to note, when considering the strengths and weaknesses of the various RANS models (discussed in Section 2.4), that Case IV is indeed also in theory one of the best choices for the airways problem. The realizable $k-\varepsilon$ model is supposed to account quite well for effects of separation and recirculation as well as curvature. All of these features are likely to be present in the airways flow. However, using any $k-\varepsilon$ model might result in exaggerated predicted turbulence, as these models do not have any damping term to lessen the turbulent viscosity to suit transitional flows. In that respect, the $k-\omega$ models might be more appropriate – such models are also supposed to work well with wall-bounded flows. However, in the simulations considered here, the $k-\omega$ models showed higher convergence residuals and less likeness to the LES data than many of the other models. The SMC models should in theory cope very well with both walls and curvature, but

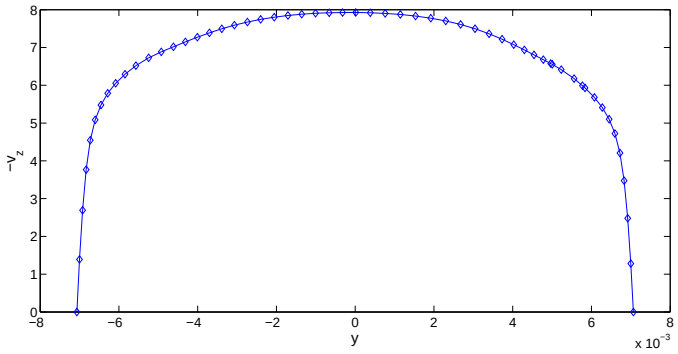

Figure 4.1: The velocity profile for the axial (z) velocity at the line $z = x = 0$ in the middle of the trachea.

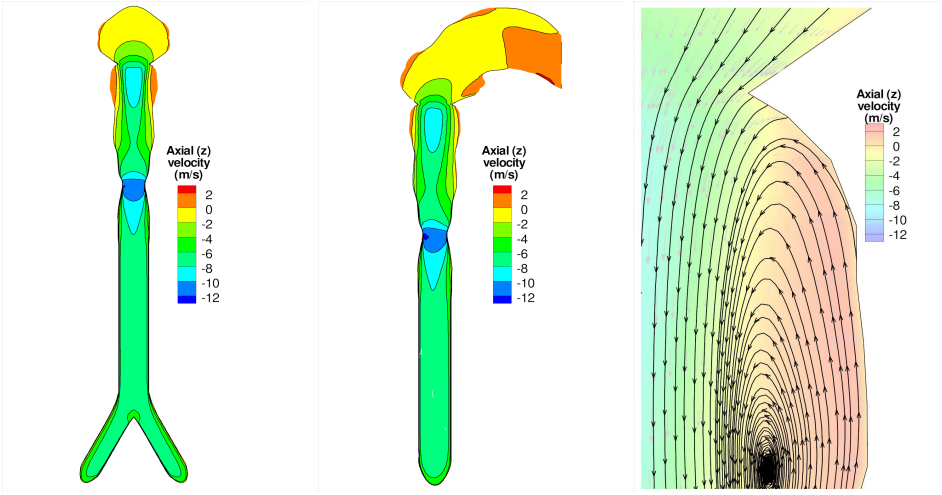

(a) (b) (c)

Figure 4.2: Contour plots of axial (z) velocity and vector plot of recirculation region.

such models might also overpredict turbulence, due to details in the model involving a turbulent viscosity formulation. Besides, SMC models are slower and harder to converge.

Note that any quantitative comparison between various models has limited or no use in this study, since it is the overall predicted behaviour of the flow which must be considered. Single values such as averages, integrals or fluxes cannot be seen isolated from the total flow field. Thus, looking at qualitative results like velocity fields or pressure distributions is a reasonable way to compare the different models.

Figure 4.1 shows the axial velocity profile for a line going through the center of a cross-section of the straight part of the trachea (between cut C and D from Figure 2.4 on page 17). As seen, the profile has the semiparabolic

shape typical for turbulent flows.

The tracheal jet below the glottis illustrated through the axial velocity in Figure 4.2(a) and 4.2(b) on the facing page is not unexpected and also agrees qualitatively with the LES results of Radhakrishan and Kassinos (2008), and others (Ball et al., 2008; Lin et al., 2007). The jet is created by the contraction at the glottis. A similar jet is seen below the epiglottis. The stagnation point at the bifurcation is worth pointing out as well. Furthermore, it can be observed that the flow direction is upwards at the walls below the epiglottis (cut B), hinting at separation and possibly a recirculation region below the epiglottis. Indeed, Figure 4.2(c) on the preceding page shows how the flow separates and circulates near the wall in this region. Note also, in Figure 4.3(c) on the following page, the secondary flows present due to the glottis (cut C). Such flows have been reported earlier by numerous researchers (Ball et al., 2008; Brouns et al., 2007; Kleinstreuer et al., 2008b). Moreover, the magnitude of this swirl, relative to the axial flow velocity, was found to be somewhat higher immediately below the glottis. Secondary flows have also been reported in the main bronchi, below the first bifurcation (Kleinstreuer et al., 2008a,b). Figure 4.4 on page 55 shows that these effects were predicted by the RANS model in this study as well.

Pressure contours at cuts A, B, C and D are displayed in Figure 4.5 on page 56, compared to those of Radhakrishan and Kassinos (2008) in the same cut planes. The pressure values from the RANS simulation are normalized to the LES data of Radhakrishan and Kassinos, in order to provide an easier comparison. Lack of access to the actual data files of Radhakrishan and Kassinos prevented normalizing both pressure fields to e.g. a range of $[0, 1]$. The normalization applied to the RANS data in Figure 4.5 on page 56 is given by

$$P_{\text{normalized}} = \frac{P - P_{\text{min}}}{P_{\text{max}} - P_{\text{min}}}(p_{\text{max-LES}} - p_{\text{min-LES}}) + p_{\text{min-LES}}$$

in which $P_{\text{normalized}}$ is the pressure from the RANS simulation normalized to the LES data, P is the actual RANS predicted pressure field, P_{max} and P_{min} are the maximum and minimum RANS pressures, respectively, for the pressure range shown in Figure 4.5 on page 56, and $p_{\text{max-LES}}$ and $p_{\text{min-LES}}$ are the maximum and minimum LES pressures, respectively, for the pressure range shown in Figure 4.5 on page 56. The values of these parameters are shown in Table 4.1.

It is clear that the contours and pressure gradients from the RANS simulations closely resemble those of the LES runs. However, the pressure level found in the present study are systematically lower than those of Radhakrishan and Kassinos (2008), perhaps due to differing simulation operating pressures between the two cases. This is, however, secondary since it is only the pressure gradient that is dynamically important.

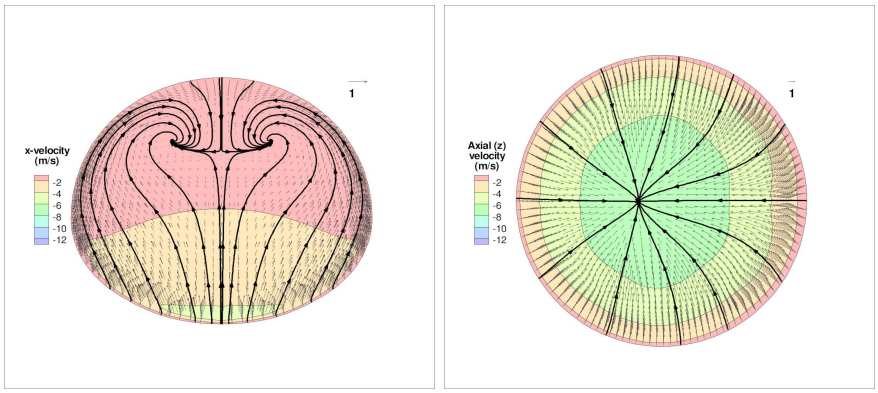

(a) Cut A.

(b) Cut B.

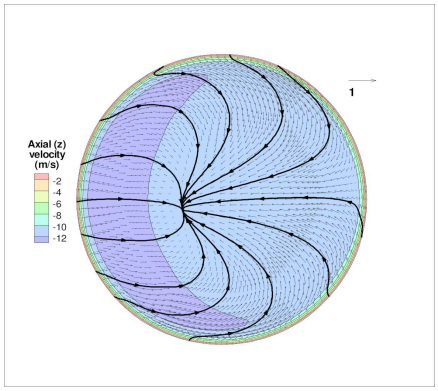

(c) Cut C.

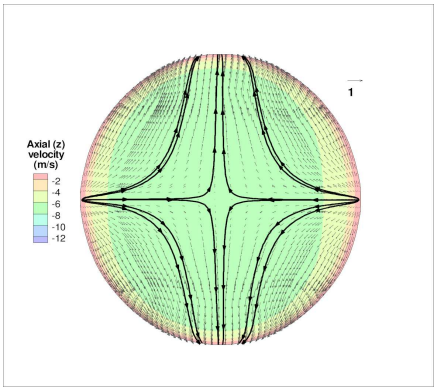

(d) Cut D.

Figure 4.3: Vector plots of velocities in the plane overlaid on contour plots of velocity perpendicular to the plane, cf. Figure 2.4 on page 17. Maximum velocity magnitude in the plane relative to the maximum velocity magnitude in the main flow direction is 20.1% (cut A), 44.2% (cut B), 4.25% (cut C) and 16.4% (cut D).

Table 4.1: A comparison of predicted pressure values (Pa)

	LES data (Radhakrishan and Kassinos, 2008)	RANS data
Maximum pressure	$p_{\text{max-LES}} = 157$	$P_{\text{max}} = 119$
Minimum pressure	$p_{\text{min-LES}} = 60.5$	$P_{\text{min}} = 57$
Pressure range	$\Delta p_{\text{LES}} = 96.5$	$\Delta P = 62$

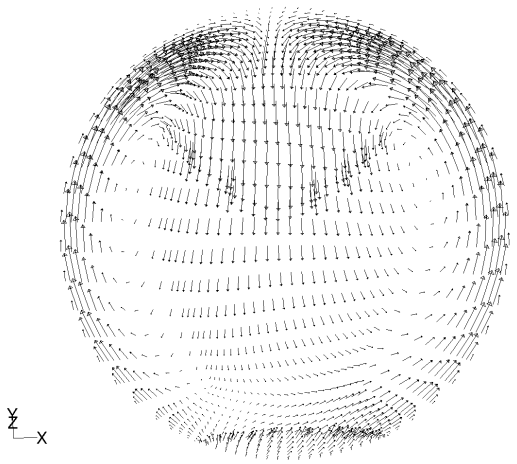

Figure 4.4: Vectors in a cut plane just below the first bifurcation. This cross-sectional cut illustrates the presence of secondary flows caused by the bifurcating flow. The vectors show velocities in the plane (m/s) and are scaled by a factor 10.

The pressure contours agree well with the velocity profiles discussed earlier. The pressure drops throughout the trachea and the pressure contours at cut D clearly indicate the coming of a bifurcation at which the flow will split almost equally between the bronchi. Note also how the pressure contours at cuts B and C are in agreement with the axial jets discussed earlier.

Finally, Figure 4.6(a) on page 58 shows the distribution of turbulence kinetic energy k. As reported by Radhakrishan and Kassinos (2008), it is seen that areas of significant turbulence are found below the glottis and epiglottis. The region below the epiglottis coincides with the recirculation region discussed earlier. In order to visualize the velocity fluctuation amplitudes compared to the mean velocity, Figure 4.6(b) on page 58 shows contours of turbulence kinetic energy per mean kinetic energy, i.e. k/K, where $K = \frac{1}{2}U_iU_i$. As seen, the velocity magnitude varies with less than 10% of its mean value almost everywhere below the glottis. However, in the upper regions, and particularly in the recirculation regions, the fluctuations are of the same order of magnitude as the velocity magnitude itself, or higher. At the core of the recirculation region below the epiglottis, the energy of the velocity flucutations are orders of ten times higher than the energy of the mean velocity. This is because at the center of the recirulation region, $|U| \to 0$. Although $|U| \to 0$, the turbulence prevails in this region since $\frac{\partial U_i}{\partial x_i} \neq 0$ in addition to diffusion/transport effects. It is beoynd doubt that such regions make particle deposition hard to predict, and that turbulence effects should definitely be accounted for when modeling flow and particle transport in the upper airways.

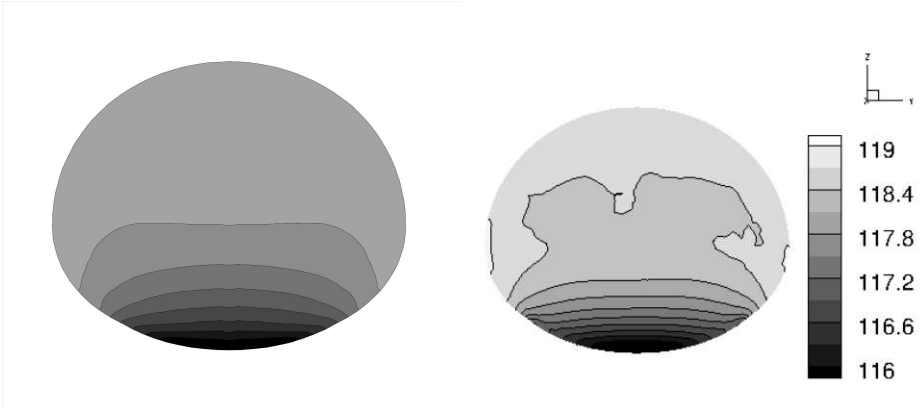

(a) Cut A: RANS Case IV data.

(b) Cut A: LES data.

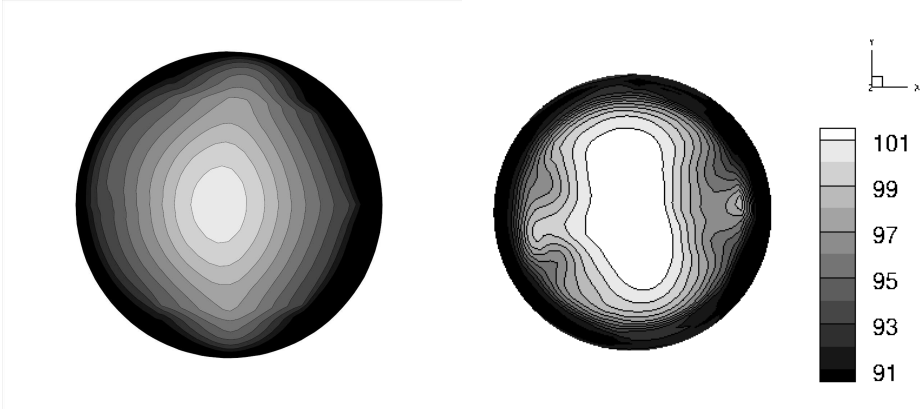

(c) Cut B: RANS Case IV data.

(d) Cut B: LES data.

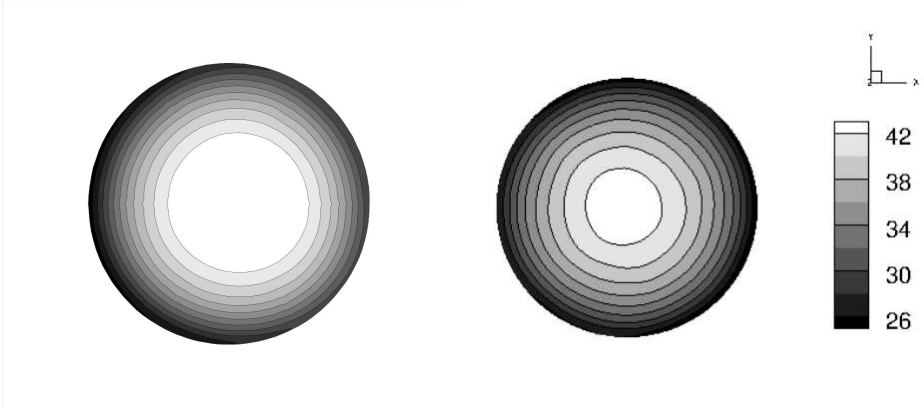

(e) Cut C: RANS Case IV data.

(f) Cut C: LES data.

Figure 4.5: Contour plots of static pressure variations, cf. Figure 2.4 on page 17 (continues on following page).

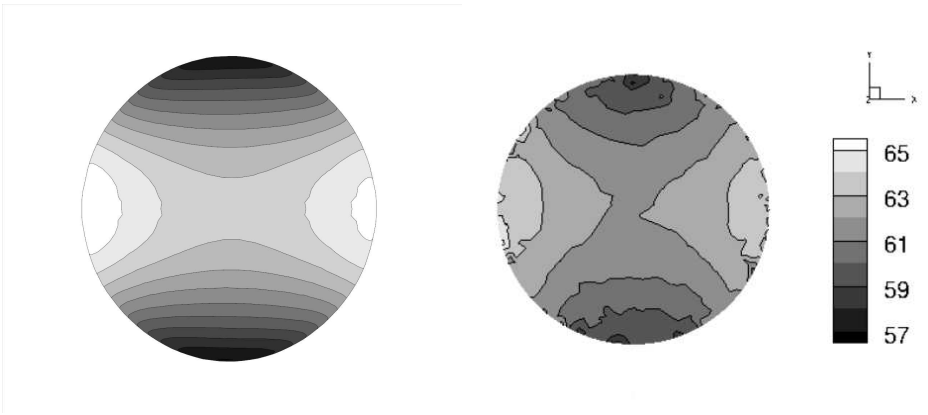

(g) Cut D: RANS Case IV data.

(h) Cut D: LES data.

Figure 4.5: Contour plots of static pressure variations, cf. Figure 2.4 on page 17 (continued from last page).

4.1.2 Particle Transport and Deposition

For the transport of the passive scalar, it was found that at $t = 0.188$ s, the entire geometry contained polluted air (more than 99,7%). An animation of the propagation was also created, in which the spreading rate and pattern can be observed in time. Not surprisingly, the polluted air propagates most rapidly in the center of the trachea, where the convection velocity is highest. Figure 4.7 on the following page shows a snapshot of the pollution spread at time $t = 0.04$ s.

When it comes to the particle deposition, statistics gathered from the Lagrangian (discrete phase) simulations are summarized in Table 4.2. It is seen that as particle sizes increase, the deposition increases dramatically. For 20 μm particles, all particles are captured at the walls, whereas for 1 μm particles, only half of the particles are trapped. The entrapment data for 10 and 20 μm particles agrees well with other computer simulations and experiments (Jin et al., 2007; Kleinstreuer et al., 2008a), but according to the same researchers, particle entrapment for 1 μm particles should be much lower than what is found in this study. Possible reasons for this include exaggerated entrapment conditions at the walls, wrongly estimated Cunningham factor, or negligence of possibly non-negligible effects such as Brownian motion. The most likely reason, however, is an overprediction of turbulence intensities. RANS models are ill-suited for regions of laminarization, and therefore the present RANS simulation may have exaggerated the effect of turbulent fluctuations on the particles, particularly in the areas below the glottis. This effect will be more dominant for smaller particles, which carry less momentum and therefore are more susceptible to variations in the flow field.

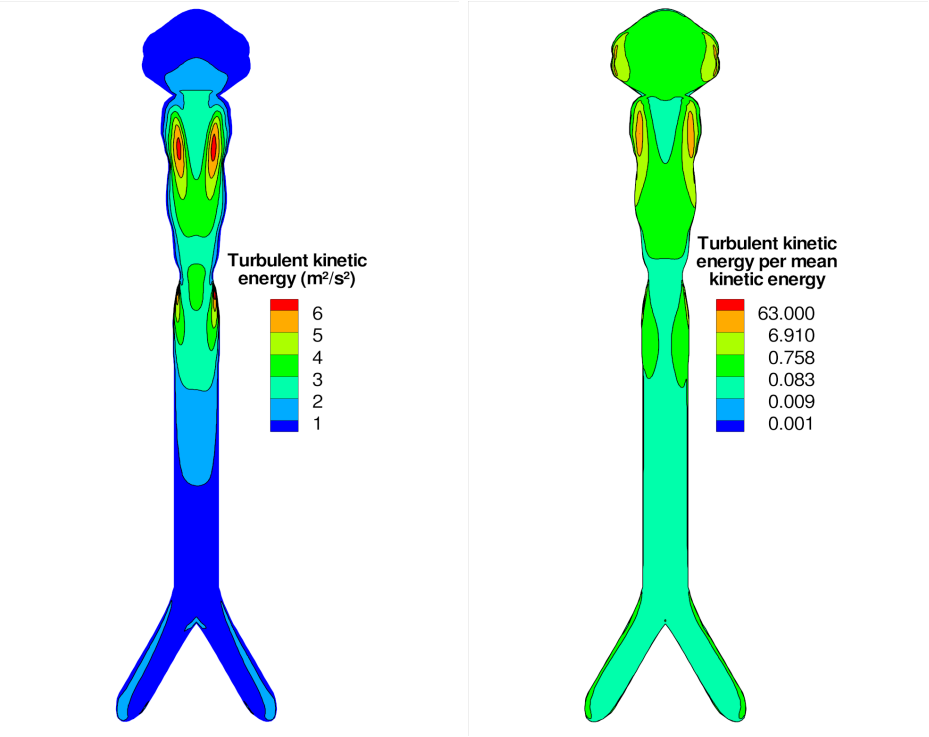

(a) Turbulence kinetic energy k.

(b) Turbulence kinetic energy per mean kinetic energy k/K.

Figure 4.6: Contours illustrating turbulence kinetic energy.

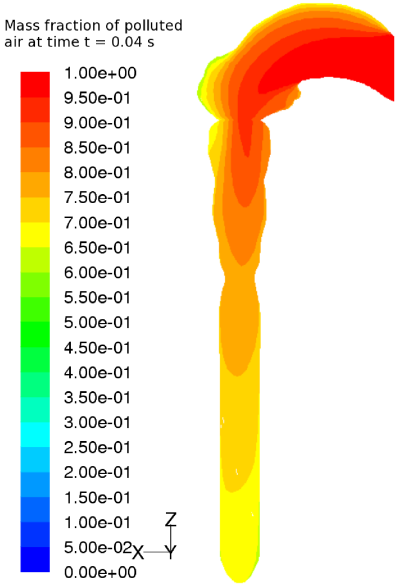

Figure 4.7: The propagation of polluted air at $t = 0.04$ s.

Table 4.2: Particle deposition summary

Particle Size	Number of particles	Deposition Rate
1 μm	4736	54.8%
10 μm	4736	97.5%
20 μm	4736	100.0%

In addition to the particle releases discussed above, a numerical simulation for 1 μm particles was done, in which turbulent fluctuations were not taken into account when computing particle tracks (i.e. the DRW model was disabled). It is interesting to note that in this simulation, the deposition efficiency was only 4.46%. Without further analysis of these data, in the least this indicates the importance of turbulence intensities on particle deposition.

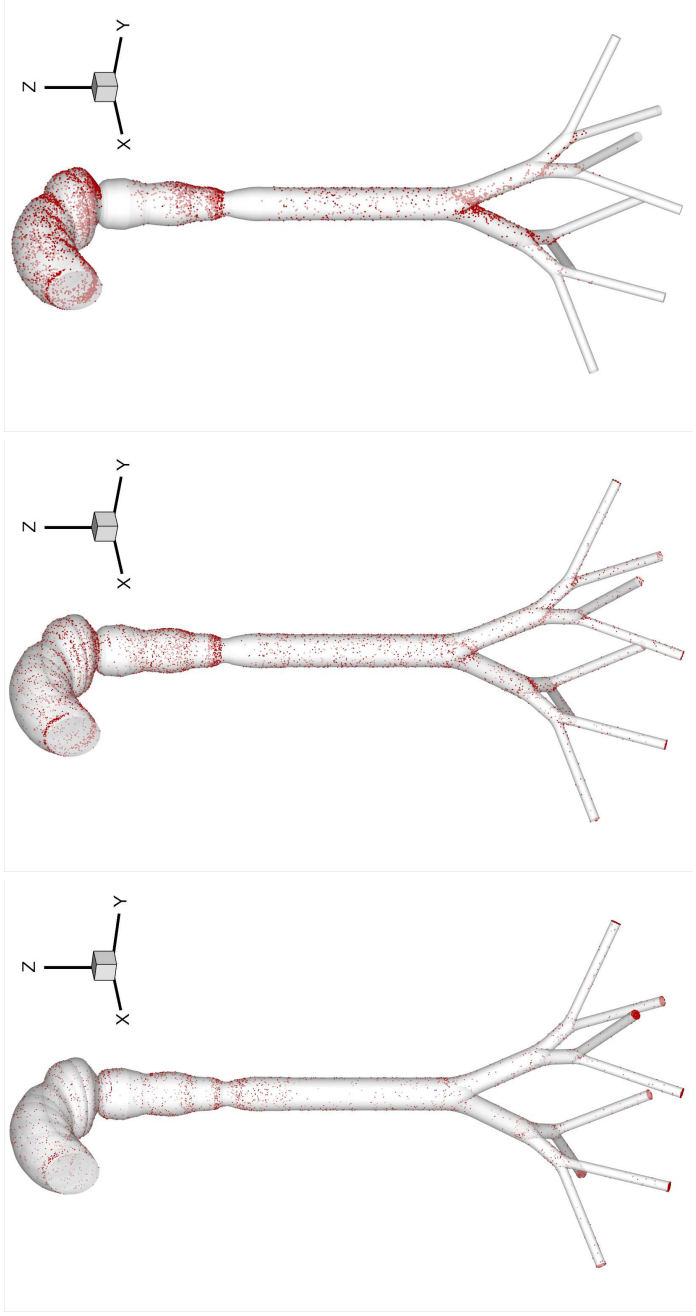

(a) 1 μm. (b) 10 μm. (c) 20 μm.

Figure 4.8: Deposition patterns for the three particle sizes simulated.

Figure 4.8 on the preceding page shows the deposition patterns for the three different particle sizes. First of all, it is clear that the deposition increases for increasing particle size, as is also shown in Table 4.2 on page 59.

Secondly, it is of interest to observe the changing deposition patterns for the varying particle sizes. Already in the oral cavity, a much larger amount of the heavier particles are deposited at the posterior wall. The larger particles have more inertia, and are therefore less inclined to follow the airflow around the sharp bend down to the trachea.

Another observation is that the deposition around the epiglottis (cut B) is more apparent for bigger particles. This might be the effect of curvature discussed above, as the deposition efficiency is particlularly high at the posterior wall, but it might also be due to the sudden narrowing of the airway at the epiglottis. The larger particles have too much momentum to follow the rapidly contracting flow, and so they hit the wall.

The glottis (cut C) also catches interest. For the 1 μm particles, two deposition "rings" can be observed by the glottis. Note that the upper ring is more dense for the heavier particles, whereas the lower ring actually disappears for such particles. This indicates two main things: Firstly, as for the epiglottis, heavier particles are more likely to be deposited at the upper part of the glottis, due to their inherent resistance to rapid airflow change. And secondly, once the airflow expands again, the inertia of the heavier particles keeps them away from the wall, whereas the light particles follow the flow more closely and are deposited. In addition to inertia effects, gravity also acts to cause the observed effects at the glottis, but the effect of gravity is minimal compared to convection at the glottis.

The last point of interest concerns the bifurcations. As is clearly seen in Figure 4.8 on the preceding page, deposition at the bifurcations is negligible for the 1 μm particles, whereas there is a substantial amount of deposition of the larger particles in this area. Again, this is caused by the inertia of the heavier particles. However, in the lower airways, from the end of the trachea and below, gravity also plays a more important role. Thus the deposition efficiency of the heavier particles increases both due to gravity and inertia. This effect is seen in all the bifurcation levels, and for the lower generations, gravity is the dominant effect. This can be seen particularly well e.g. in the lowest bifurcations of the 20 μm particle simulation, in which deposition is only on one side of a bifurcation, i.e. on the lower side.

When comparing these results to those of Radhakrishan and Kassinos (2008), which only include deposition in the lower airways, there are two main differences. Firstly, the LES simulation of Radhakrishan and Kassinos predicts less deposition on the straight parts of the trachea and bronchi walls. This might indicate that there is a difference in the prediction of turbulence kinetic energy between the LES and the RANS model. The latter is much more likely to overpredict the intensity, which provides a plausible explanation of the observed difference in particle deposition.

The second difference regards the deposition in the bifurcations. Radhakrishan and Kassinos (2008) show a considerable deposition even for the 1 μm particles, whereas the results from the present study predicts no such deposition, similar to the study of e.g. Jin et al. (2007). Due to the stagnation point at the bifurcation (see Figure 4.2 on page 52), it would seem reasonable for the light particles, which follow the flow, not to become easily entrapped at the bifurcation. It is possible that the LES grid of Radhakrishan is too coarse in this region, which would ease the entrapment of particles. This could explain the observed difference. Another explanation is simply that the LES simulations injected more particles, thus making the deposition more apparent in all parts of the geometry. Finally, the reason may be related to the swirling jet in the trachea, discussed in Section 4.1.1. This jet has been completely dissolved at the bifurcation in the RANS simulations. In the LES simulations, on the other hand, the swirling jet is present all the way down to the epiglottis (Radhakrishan and Kassinos, 2009). Such a jet might increase particle deposition at the bifurcation.

The data shown in Figure 4.8 on page 60 was obtained through a rather laborious manner. The Discrete Phase Model was used in Fluent, and for each time step, every particle's position was written to a file. Several files had to be created to avoid excessive file sizes. The particle files were then modified manually a little bit, to suit the format required for MATLAB. Then, the files were read into MATLAB, at which point a small algorithm picked out all coordinates at which any particle ended its trajectory. These «end point coordinates» were then exported to a new file, which was read into the graphical plotting program Tecplot. Finally, in Tecplot the three-dimensional geometry of the airways was coupled with the end point coordinate file to create the figures shown here. The MATLAB script is included in Appendix A.

4.2 Transient Solutions

4.2.1 Airflow

Not much time has been spent on the transient simulations. It has been established that unsteady RANS is easy to implement in the commercial solver Fluent. It is, however, harder to find a converged solution than for the steady state simulations.

Figure 4.9 on the facing page shows two snapshots of the time-developing velocity field. The first time is during inhalation and the second time is during exhalation. For the inspirational case ($t = 0.30$ s), it is seen that the velocity field is beginning to approach the field predicted in the steady state simulations. For the expirational case ($t = 1.71$ s), the flow is clearly reversed. Thus, a jet develops above the glottis and epiglottis instead of below, and some swirls are produced in the oral cavity.

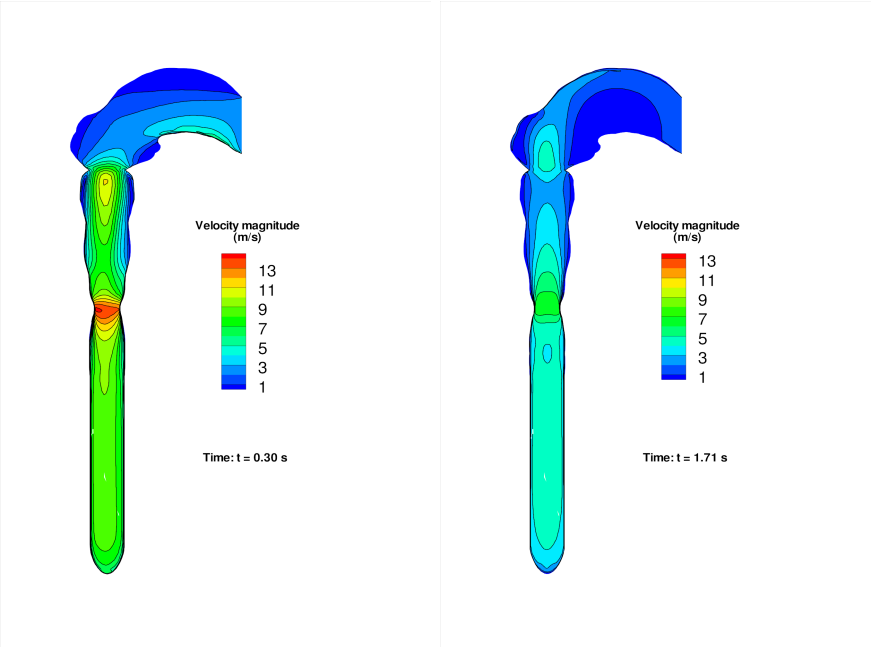

(a) $t = 0.30$ s. (b) $t = 1.71$ s.

Figure 4.9: The unsteady mean velocity magnitudes.

It is clear that more studies of transient breathing cycles should be conducted; even though the velocities are generally lower than for the steady state case, the change in flow direction may produce other – and perhaps even more pronounced – turbulence effects than the steady state flow.

4.2.2 Scalar Transport

Only scalar transport has been considered for the transient airflow. It is likely that only the inspirational part of the breathing cycle provides reliable data, since the boundary conditions may be wrong for the expirational breathing, during which the original outlets of the bronchi become inlets.

Scalar transport in transient airflow was difficult to simulate, mainly due to problems with obtaining a converged solutions. The solver in Fluent did particularly struggle when the inhalation turned to exhalation, i.e. at halfway through a breathing cycle. This is probably connected to «division by zero»-like problems in the numerical solver.

In any case, Figure 4.10 on the next page shows the distribution of polluted air in the lungs at time $t = 0.30$ s. Note that the distribution is somewhat similar to that of the steady state case (Section 4.1.2), but that the time spent to reach such a distribution is much longer. This is not unexpected, since the steady state case was computed for the maximum velocity, a velocity which is not reached until about $t = 1.57$ s in the transient case.

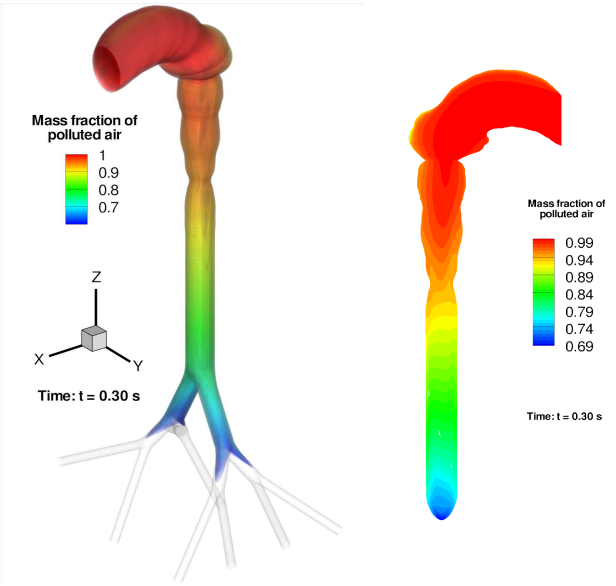

(a) 3D illustration. (b) 2D illustration.

Figure 4.10: The propagation of polluted air at $t = 0.30$ s.

Nevertheless, it is seen that the polluted air quite rapidly spreads into the bronchi. At $t = 0.50$ s, more than 99% of the geometry was filled with polluted air. The simulation also suggests that the polluted air is quite quickly pushed out of the lungs again during exhalation – but as mentioned, the results of the simulated exhalation might not be entirely correct. Note, finally, that the propagation of the polluted air in a given cut plane is more even in the transient case than in the steady state case. In the latter, the distribution of concentration in a cut plane is much more paraboloidic.

Since the propagation of a passive scalar is slower in cyclic breathing than for the steady state case, particle deposition is likely to be lower in reality than predicted by the steady state case.

5 Conclusions

My work with this thesis has given me valuable insight into turbulence modeling, especially related to Reynolds-Averaged Navier-Stokes (RANS) models. It is clear that although RANS models may be replaced by Large Eddy Simulations (LES) or Direct Numerical Simulations (DNS) computations in many cases – especially as computer capabilities expand – RANS models provide a quicker way of predicting turbulent flows. In this study, it has been seen that RANS can capture most aspects of the mean flow, even for flows in complicated geometries. Thus RANS models are useful for industrial purposes and in cases where the geometries are too complex (or large) for LES or DNS to converge in reasonable time. An additional drawback of LES and DNS is that, even with unlimited computer power, boundary conditions are harder to specify than for RANS modeling.

The literature study conducted in connection with this paper has revealed that CFD applied to biomedical flows has vast room for improvement. Most research so far uses idealized geometries, limited particle transport models and often simplified turbulence models. Besides, aspects related to the numerical methods can probably be improved. As computing power increases and more advanced mathematical models emerge, cases such as that studied in the present paper can be expanded in numerous ways, as will be discussed shortly.

Most of the RANS models investigated in the present study showed convincing results for the flow field. Case I contained less information than the other scalar models, and case IX produced unreasonable results. The reason for this failure is unknown, but it is suspected that the near-wall treatment in the model of case IX is inadequate for such low Reynolds number flow considered here. Otherwise all the closure models could have been used to predict particle transport. Case IV was chosen for the particle transport models, as this scalar model resembled the tensor models and the LES data of Radhakrishan and Kassinos (2008) marginally more than the other mod-

els.

The predicted mean flow field was in close agreement with the LES data (Radhakrishan and Kassinos, 2008) on most accounts. The tracheal jet, secondary flows and stagnation points predicted by other researchers were also present in the RANS model used in this study. A recirculation region below the epiglottis was also predicted. The most notable difference between the LES and the RANS data was the prediction of turbulence kinetic energy, particularly for the low turbulence regions.

The particle deposition showed that the deposition rate increased with increased particle size. While this is in agreement with other studies, the predicted deposition efficiency for the 1 μm particles was nevertheless higher in the present study than reported by others. The deposition patterns showed that inertia affects deposition dramatically. Gravity also has an effect on heavier particles in the bronchi. Deposition in the oral cavity and bifurcations increases particularly much with particle size. These results concur with other studies.

Concerning the time-dependent solution, it has been shown that unsteady RANS modeling is possible, although harder to converge, in Fluent. Transient simulations probably give more realistic predictions of the airflow, and turbulence effects might differ from the steady state case. Propagation of a passive scalar is slower in a sinuous breathing cycle than for a steady state inspirational flow, and therefore particle deposition in the unsteady flow will probably be lower than for the steady state case.

It is evident that a lot of future work related to flow and particle transport in the airways should be done. The respiratory system constitutes a complex geometry, and numerous improvements on the geometry used in the current study could be introduced. The effects of unsteady breathing should definitely be investigated, as should a broader range of particle sizes and densities. Effects of temperature and two-way coupling with the continuous phase ought to be studied as well. And finally, the challenge of predicting laminarization using RANS models persists.

Bibliography

Ball, C. G., Uddin, M., and Pollard, A. High resolution turbulence modelling of airflow in an idealised human extra-thoracic airway. *Computers & Fluids*, 37:943–964, 2008.

Britannica Concise Encyclopedia. Respiratory system. 1994–2008. URL `http://encyclopedia2.tfd.com/respiratory+system`.

Brouns, M., Verbanck, S., and Lacor, C. Influence of glottic aperture on the tracheal flow. *Journal of Biomechanics*, 40:165–172, 2007.

Caro, C. G., Schroter, R. C., Watkins, N., Sherwin, S. J., and Sauret, V. Steady inspirational flow in planar and non-planar models of human bronchial airways. *Proceedings of the Royal Society of London A*, 458:791–809, 2002.

Cheng, Y.-S., Zhou, Y., and Chen, B. T. Particle deposition in a cast of human oral airways. *Aerosol Science and Technology*, 31:286–300, 1999.

Comer, J. K., Kleinstreuer, C., and Zhang, Z. Flow structures and particle deposition patterns in double-bifurcation airway models, part 1. Airflow fields. *Journal of Fluid Mechanics*, 435:25–54, 2001a.

Comer, J. K., Kleinstreuer, C., and Zhang, Z. Flow structures and particle deposition patterns in double-bifurcation airway models, part 2. Aerosol transport and deposition. *Journal of Fluid Mechanics*, 435:55–80, 2001b.

Dahl, H. A. and Rinvik, E. *Menneskets funksjonelle anatomi, 3. utgave* (J. W. Cappelens Forlag AS, Oslo, Norway, 2007).

Durbin, P. A. and Petterson Reif, B. A. *Statistical Theory and Modeling for Turbulent Flows* (John Wiley & Sons Ltd, West Sussex, England, 2003).

Fluent 6.3 User's Guide. *Fluent 6.3 User's Guide* (Fluent, Inc., New Hampshire, USA, 2006).

Gibson, M. M. and Launder, B. E. Ground effects on pressure fluctuations in the atmospheric boundary layer. *Journal of Fluid Mechanics*, 86:491–511, 1978.

Jin, H. H., Fan, J. R., Zheng, M. J., and Cen, K. F. Large eddy simulation of inhaled particle deposition within the human upper respiratory tract. *Aerosol Science*, 38:257–268, 2007.

Kleinstreuer, C., Zhang, Z., and Li, Z. Modeling airflow and particle transport/deposition in pulmonary airways. *Respiratory Physiology & Neurobiology*, 163:128–138, 2008a.

Kleinstreuer, C., Zhang, Z., Li, Z., Roberts, W. L., and Rojas, C. A new methodology for targeting drug-aerosols in the human respiratory system. *Jornal of Heat and Mass Transfer*, 51:5578–5589, 2008b.

Kundu, P. K. and Cohen, I. M. *Fluid Mechanics, Fourth Ed.* (Academic Press, USA, 2008).

Launder, B. E. Second-moment closure and its use in modeling turbulent industrial flows. *International Journal for Numerical Methods in Fluids*, 9:963–985, 1989a.

Launder, B. E. Second-moment closure: Present... and future? *International Journal of Heat and Fluid Flow*, 10 (4):282–300, 1989b.

Launder, B. E. and Spalding, D. B. *Lectures in Mathematical Models of Turbulence* (Academic Press, London, England, 1972).

Lin, C.-L., Tawhai, M. H., McLennan, G., and Hoffman, E. A. Characteristics of the turbulent laryngeal jet and its effects on airflow in the human intro-thoracic airways. *Respiratory Physiology & Neurobiology*, 157:295–309, 2007.

Liu, Y., So, R. M. C., and Zhang, C. H. Modeling the bifurcating flow in a human lung. *Journal of Biomechanics*, 35:465–473, 2002.

Menter, F. R. Two-equation eddy-viscosity turbulence models for engineering applications. *AIAA Journal*, 32 (8):1598–1605, 1994.

Pope, S. B. *Turbulent Flows* (Cambridge University Press, Cambridge, United Kingdom, 2000).

Radhakrishan, H. and Kassinos, S. Using LES to model turbulent particle transport in the airways of the human respiratory system. *Proceedings of the 7th International Symposium on Engineering and Turbulence Modelling and Measurements*, 3:857–862, 2008.

Radhakrishan, H. and Kassinos, S. On recent LES computations. Private communication, 2009.

Sand, O., Sjaastad, Ø. V., and Haug, E. *Menneskets fysiologi* (Gyldendal Norsk Forlag, Oslo, Norway, 2007).

Shih, T. H., Liou, W. W., Shabbir, A., Yang, Z., and Zhu, J. A new $k-\varepsilon$ eddy-viscosity model for high Reynolds number turbulent flows – model development and validation. *Computers Fluid*, 24 (3):227–238, 1995.

Slack, M. The ins & outs of breathing. *Fluent News*, p. 17, 2005.

Spalart, P. and Allmaras, S. A one-equation turbulence model for aerodynamic flows. *Tech. Rep. AIAA-92-0439, American Institute for Aeronautics and Astronautics*, 1992.

Su, L. K. and Mungal, M. G. Simultaneous measurements of velocity and scalar fields: Application in crossflowing jets and lifted jet diffusion flames. In *Center for Turbulence Research Annual Briefs* (Stanford University, 1999).

Weibel, E. R. *Morphometry of the Human Lung* (Springer Verlag, Berlin, Germany, 1963).

White, F. M. *Viscous Fluid Flow, Third Ed.* (The McGraw-Hill Companies, New York, USA, 2006).

Wilcox, D. C. *Turbulence Modeling for CFD* (DCW Industries, Inc., California, USA, 1998).

Wolfstein, M. The velocity and temperature distribution of one-dimensional flow with turbulence augmentation and pressure gradient. *International Journal of Heat and Mass Transfer*, 12:301–318, 1969.

Yakhot, V. and Orszag, S. A. Renormalization group analysis of turbulence: I. Basic theory. *Journal of Scientific Computing*, 1 (1):3–51, 1986.

Zhang, Z. and Kleinstreuer, C. Airflow structures and nano-particle deposition in a human upper airway model. *Journal of Computational Physics*, 198:178–210, 2004.

Appendix

A Computer Code

A.1 C++

The transient inlet velocity of the unsteady RANS simulations were implemented with the following C++ code, used in conjunction with the Fluent User-Defined Function libraries.

```
#include "udf.h"

#define UMAX 4.8361
#define RADIUS 0.01147343433
#define YC 0
#define ZC 0.1020012
#define T 1.57079633

DEFINE_PROFILE(vel_prof_t,t,i) {
        real pos[ND_ND];
        real y;
        real z;
        face_t f;
        real a;
        real tid = CURRENT_TIME;

        a = sqrt(UMAX/(RADIUS*RADIUS));

        begin_f_loop(f,t)
        {
                F_CENTROID(pos,f,t);
                y = pos[1];
                z = pos[2];
                F_PROFILE(f,t,i) = UMAX*sin(2*tid);
        }
        end_f_loop(f,t)
}
```

A.2 MATLAB

The following code picks out end points from particle trajectories and writes them to a vector. After executing this script, the three resulting vectors are written to an ASCII file that can be read into the plotting program Tecplot.

```
% For N particle tracks given by coordinates px, py, pz and time
    t, this
% file summarizes the tracks' endpoints in three vectors x, y, z
    .

c = 1; % Counter
T = length(t);
t(T+1) = 0; % Adds a last point of zero to t to include last
    particle track

for j = 1:T
    if t(j+1) < t(j) % A particle track ends if time t is reset.
        life(c) = t(j); % Particle life time
        x(c) = px(j); % Particle endpoint's x-coord
        y(c) = py(j); % Particle endpoint's y-coord
        z(c) = pz(j); % Particle endpoint's z-coord
        c = c+1;
    end
end

x = transpose(x);
y = transpose(y);
z = transpose(z);
COORD = [x y z];
```